SURFACE STRUCTURING OF ADVANCED MATERIALS AT ROOM TEMPERATURE ON A BENCHTOP

by
ELİF FERLİGÜL

Submitted to the Graduate School of Engineering and Natural Sciences in partial fulfillment of the requirements for the degree of Master of Science

Sabancı University

June 2025

SURFACE STRUCTURING OF ADVANCED MATERIALS AT ROOM TEMPERATURE ON A BENCHTOP

Approved by:

Prof. Dr. Özge Akbulut …….
(Thesis Supervisor)

Prof. Dr. Yusuf Ziya Menceloğlu …….....

Prof. Dr. Ozan Akdoğan ……...

Date of Approval: June 19, 2025

ABSTRACT

SURFACE STRUCTURING OF ADVANCED MATERIALS AT ROOM TEMPERATURE ON A BENCHTOP

ELİF FERLİGÜL

MATERIAL SCIENCE AND NANO ENGINEERING MSc. THESIS, JULY 2025

Thesis Supervisor: Prof. Dr. ÖZGE AKBULUT

Keywords: Inconel 718, PVA, surface structuring/patterning/texturing, benchtop, near-net shaping

Currently, near-net shaping of advanced materials, such as Inconel 718, is performed using energy-intensive methods that require specialized and costly equipment. Additionally, the most advanced additive manufacturing methods can only process one workpiece at a time, leading to longer work times that are not suitable for large-scale production. This study proposes a method for forming a green body of Inconel 718 powder through the use of polyvinyl alcohol (PVA) via homogeneous coagulation in water. The as-prepared green body has a dough-like rheology and it could be shaped by hand or pushed into a mold eliminating the hurdles, such as waiting for the evaporation of water in slip casting. Furthermore, the dough-like rheology allows the application of patterns onto the metal surface via stamps, wheels, or rollers with forces that are on the order of 10 N. The use of self-standing and malleable metal dough systems enables the creation of customized geometries with high fidelity in a short time, without the need for specialized and costly equipment, at room temperature and atmospheric pressure. This study establishes a foundational basis for this method and paves the way for further advancements in the process, rendering it accessible even in frugal environments for individuals and SMEs without domain knowledge and with limited equipment.

ÖZET

TEZGÂH ÜSTÜ, ODA SICAKLIĞINDA GELİŞMİŞ MALZEMELERİN YÜZEY YAPILANDIRMASI

ELİF FERLİGÜL

MALZEME BİLİMİ VE NANOMÜHENDİSLİĞİ YÜKSEK LİSANS TEZİ, TEMMUZ 2025

Tez Danışmanı: Prof. Dr. ÖZGE AKBULUT

Anahtar Kelimeler: Inconel 718, PVA, yüzey yapılandırma/desenleme/dokulama, tezgâh üstü, nihai şekle yakın üretim

Günümüzde, Inconel 718 gibi gelişmiş malzemelerin net şekillendirmeye yakını, özel ve maliyetli ekipman gerektiren yoğun enerjili yöntemler kullanılarak gerçekleştirilmektedir. Ek olarak, en gelişmiş eklemeli imalat yöntemleri, bir seferde yalnızca bir iş parçasını işleyebilir ve bu da büyük ölçekli üretim için uygun olmayan daha uzun çalışma sürelerine yol açar. Bu çalışma, suda homojen koagülasyon yoluyla polivinil alkol (PVA) kullanımı ile Inconel 718 tozunun yeşil gövdesini oluşturma yöntemini önermektedir. Hazırlanan yeşil gövdenin hamur benzeri bir reolojisi vardır ve elle şekillendirilebilir veya bir kalıba itilebilir, böylece slip dökümde suyun buharlaşmasını beklemek gibi engeller ortadan kaldırılabilir. Ayrıca, hamur benzeri reoloji, 10 N mertebesinde kuvvetlerle damgalar, tekerlekler veya silindirler aracılığıyla desenlerin metal yüzeye uygulanmasına izin verir. Kendi kendine duran ve şekillendirilebilir metal hamur sistemlerinin kullanımı, oda sıcaklığında ve atmosfer basıncında, özel ve pahalı ekipmanlara ihtiyaç duyulmadan kısa sürede yüksek doğrulukla özelleştirilmiş geometrilerin oluşturulmasını sağlar. Bu çalışma, bu yöntem için bir temel oluşturur ve süreçte daha fazla ilerlemenin yolunu açar, sınırlı alan bilgisi ve ekipmana sahip olan bireyler ve KOBİ'ler için bu yöntemi imkânların kısıtlı olduğu bir ortamda dahi erişilebilir hale getirir.

ACKNOWLEDGEMENTS

I would like to express my gratitude to my supervisor Prof. Dr. Özge Akbulut, for her support during my master's studies. She provided guidance not only to my academic studies but also to my career development. She's a true inspiration due to her endless energy, ability to handle multiple tasks simultaneously, and creative problem-solving skills, even in the most challenging situations. Moreover, she always pays close attention to our questions and provides prompt answers.

I would like to extend my appreciation to my jury members, Prof. Dr. Yusuf Ziya Menceloğlu and Prof. Dr. Ozan Akdoğan for allocating their precious time.

I would like to thank my research group: Burçin Gül Üstbaş, Ayşe Ay, İleyna Sevde Üvak, and Öykü Yanaz for their help with experiments and their support.

During this time, I want to extend special thanks to the FENS Laboratory Specialists: Cansu Yılmaz Baker, Bilge Esenkal, Anıl Tez, and İlker Sevgen. They shared their expertise on characterization instruments and provided suggestions to improve my experimental setup, offering support to meet any related needs. Additionally, I would like to thank Co-Space members Muhammed Ali Bayraktar and Onur Çırakoğlu for their assistance with technical drawings and 3D printed objects.

Lastly, I'm truly thankful to my loving family for their ongoing support and encouragement. This thesis would not have been possible without the continuous support of my beloved fiancé, Uğur Sökmen; my mother, Hatice Ferligül; my father, Süleyman Ferligül; and my brother, Yunus Emre Ferligül. I have always felt deep in my heart that you are always with me, no matter where I am or when, and this feeling has given me the strength to continue on my way, no matter how difficult the road may seem.

I would like to conclude my gratitude with two sayings that give me hope when circumstances feel overwhelming. As my mother always says, “Starting is half done,” and as my father often reminds me, “The time when darkness is the most intense is when light is closest.”. Their words continue to guide me through challenges and remind me that perseverance begins with a single step.

To my dear family and my lovely fiancé Uğur

TABLE OF CONTENTS

LIST OF TABLES

LIST OF FIGURES

LIST OF ABBREVIATIONS

CNC	:	Computer Numerical Control
DED	:	Directed Energy Deposition
EBM	:	Electron Beam Melting
EDM	:	Electrical Discharge Machining
EDS	:	Energy-Dispersive X-ray Spectroscopy
ESR	:	Electroslag Remelting
G’	:	Storage Modulus
G’’	:	Loss Modulus
HIP	:	Hot Isostatic Pressing
IN718	:	Inconel 718
LPBF	:	Laser Powder Bed Fusion
LVER	:	Linear viscoelastic region
PSA	:	Particle Size Analysis
PVA	:	Polyvinyl alcohol
SEM	:	Scanning Electron Microscope
SLM	:	Selective Laser Melting
TGA	:	Thermogravimetric Analysis
VAR	:	Vacuum Arc Remelting
VIM	:	Vacuum Induction Melting
XRD	:	X-ray Diffraction

LIST OF SYMBOLS

F_{max}	:	Maximum force at the break in N
σ	:	Bending stress in MPa
b	:	Width of the sample in mm
d	:	Thickness of the sample in mm
L	:	Span length for the support in mm

CHAPTER 1

1. INTRODUCTION

Microscale surface structuring of metals involves deliberately modifying metal surfaces to create micrometer-sized features like grooves, ridges, pits, or pillars. Micro-level topographic patterns impart specialized surface properties, promoting adhesion and altering wettability for self-cleaning and anti-icing applications (Arzt et al., 2021). They can also improve coatings for paints (Arzt et al., 2021), reduce friction and wear by decreasing the contact area and increasing lubrication (S. Liu et al., 2022), and lead to high corrosion resistance (Khaskhoussi et al., 2021). Additionally, they can refine optical properties by controlling light reflection and scattering, creating plasmonic effects (Zhou et al., 2022). Moreover, they can improve biocompatibility and antibacterial properties for implants (Shan et al., 2019). Many examples are available from plants and animals in nature: for example, the lotus leaves have roughness on their surface, giving them superhydrophobic and self-cleaning properties (Figure 1.1) (Koch et al., 2009).

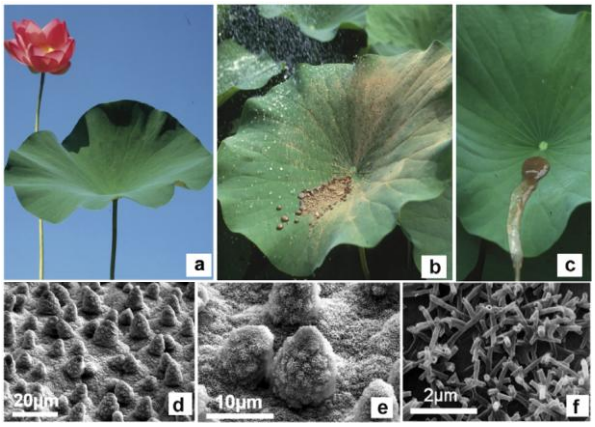

Figure 1.1. (a) Lotus plant, (b-c) The self-cleaning property of the lotus leaves, (d-f) SEM micrographs of lotus leaves (Koch et al., 2009)

The denticles on the shark skin reduce the drag in fluid flow and prevent bio-fouling, provide protection, and adapt for bioluminescence (Bixler & Bhushan, 2012, 2013; Ghimire et al., 2024). These riblet-shaped denticles can be seen in Figure 1.2.b.

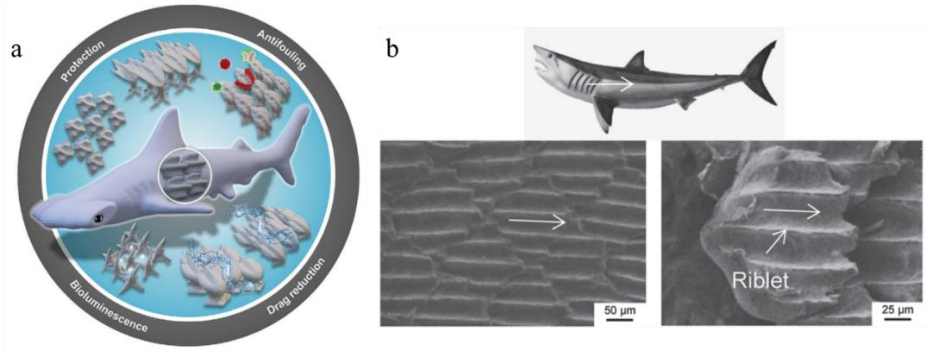

Figure 1.2. (a) Shark denticles for specific functions (Ghimire et al., 2024), (b) Actual shark skin sample from *Mako, Isurus oxyrinchus* (Bixler & Bhushan, 2012, 2013)

These highly functionalized micro-structured surfaces observed in nature inspire engineering applications and are replicated in many fields, such as optics, electronics, precision mechanics, biomedical devices, aerospace, and defense industries (Ma et al., 2023; Song et al., 2023). In this chapter, surface structuring of metals from the perspective of purposes and applications will be explained by examples from the abovementioned fields. Then, the current methods to texture the metal surfaces will be introduced, along with their advantages and disadvantages.

1.1. Surface Structuring of Metals: Purposes and Applications

Surface structuring can improve the mechanical, thermal, chemical, and optical properties of materials, as well as their biocompatibility, by modifying their surface morphology and structure (Song et al., 2023). In the aspect of mechanical properties, surface roughening or texturing on a micro-scale has been extensively utilized for energy savings by reducing friction in many machine equipment parts (Wei et al., 2021), such as cutting tools (Sugihara & Enomoto, 2009), bearings (Tala-Ighil et al., 2007), cylinders (Yin et al., 2022), pistons (J. Zhang et al., 2018), and rotating shafts (Sinanoğlu et al., 2005). For example, tribological properties, which describe the behavior of materials regarding friction, wear, and lubrication during surface contact motion, can be reinforced by reducing friction and wear through micro-scale grooves or dimple patterns on metals such

as steel (Wu et al., 2021). Micrometer-sized rectangular dimples on EN31 steel (Figure 1.3) reduce the friction coefficient and friction-related noise (John & Hanief, 2023). Another study on stainless steel reported that incorporating surface microstructures can decrease friction vibration by 95%, friction coefficient by 27%, and friction noise by 66% compared to the smooth surface (S. Liu et al., 2022).

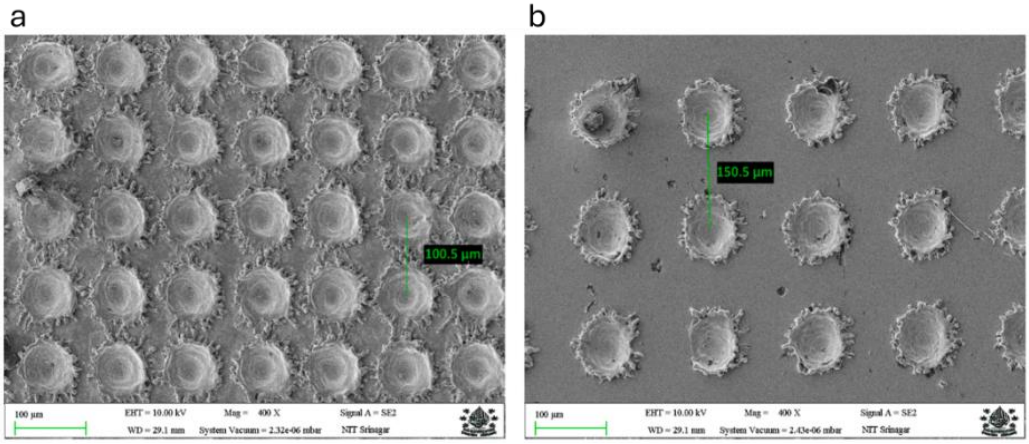

Figure 1.3. Structured surfaces of EN31 steel: (a) 100 µm and (b) 150 µm dimple pitch (John & Hanief, 2023)

Structured surfaces can be engineered for thermal and chemical applications, in addition to providing mechanical enhancements. 6082 aluminum alloy was chemically etched to form microscale platelets (length of about 2 µm) and nanoscale pits (dimension lower than 150 nm) for superhydrophobic behavior (Khaskhoussi et al., 2021) to increase the corrosion resistance of aluminum alloys. An example for the thermal application can be given from the micro-channels or rough surfaces designed to accelerate heat transfer in heat exchangers. Copper surface was biomachined with *Acidithiobacillus ferooxidans* bacteria to form approximately 250 µm depth micro channels (Figure 1.4.a), which resulted in higher pressure drop and heat transfer rate (Taufiqurrakhman et al., 2021). Another important field where the micro-range surface geometries interacting with the incident light to form color patterns play an essential role is optics. Periodic structures on Chromium (Cr) metal (Figure 1.4.b) lead to structural colors due to the anisotropic diffraction of white light, with the potential applications for anti-counterfeiting and optical sensors (Zhou et al., 2022).

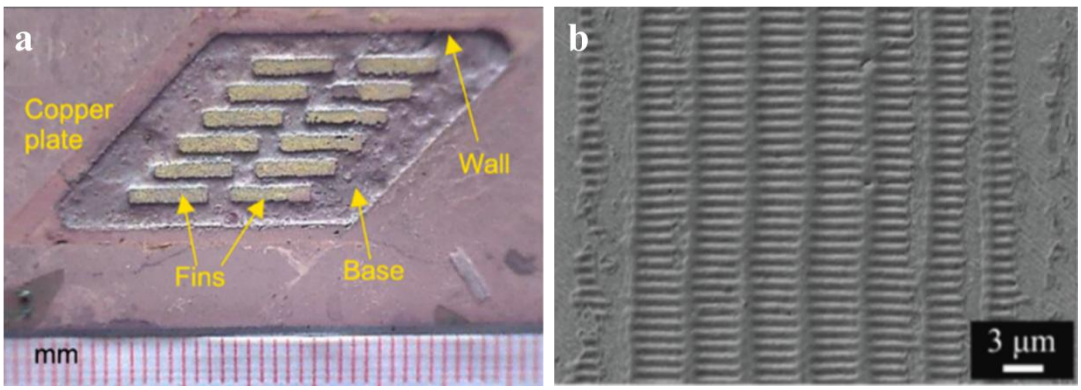

Figure 1.4. (a) Biomachined copper plate with 250 µm depth micro channels (Taufiqurrakhman et al., 2021), (b) The periodic structures on the Cr metal that diffract the light anisotropically (Zhou et al., 2022)

Surface texturing can augment the biocompatibility of metals. For instance, microstructures on a biomedical implant can remediate the response of tissues and fasten the conjugation of implants with the tissue, known as osseointegration. Titanium (Ti) metal, which has outstanding cytocompatibility, good mechanical properties, and corrosion resistance, provides better osseointegration when its surface is roughened at the microscale (Figure 1.5) (Shan et al., 2019).

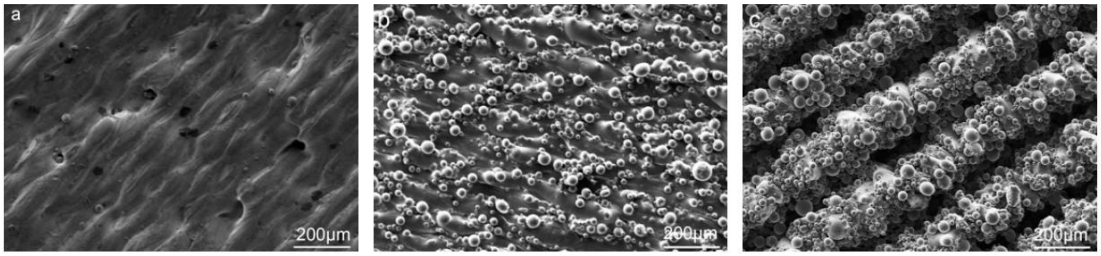

Figure 1.5. (a) Stripy, (b) Bulbous, and (c) Bulbous-stripy composite surface structure of Ti implants (Shan et al., 2019)

All these examples showed that the necessity of surface texturing at the microscale arises from the unique functional improvements in the material itself. The pattern in which metal surfaces are structured depends on the specific requirements of the application and the inherent properties of the materials. The purpose can be to decrease friction, control wettability, improve heat transfer, increase biocompatibility, and provide aesthetic or optical properties to a metal surface. In the following section, the methods for surface structuring of metals will be explained.

1.2. Methods for Surface Structuring of Metals

Surface structuring of metals at the micro scale is a challenge in manufacturing because it requires small dimensions and complex geometries. Additionally, it is not straightforward to produce such nuanced features on materials with high melting temperatures and strength using conventional methods. Conventional manufacturing methods are based on heat treatments, such as vacuum induction melting (VIM), vacuum arc remelting (VAR), electroslag remelting (ESR), hot working processes, and hot isostatic pressing (HIP). These methods require costly investments and high operational expenses, and their ability to create complex features is limited since they rely on volume-based production and tool sizes (Ullah et al., 2025). Thus, many specialized manufacturing methods have been developed to overcome the limitations of the conventional methods. The modern techniques to manufacture micro features can be listed as photolithography-based processing, computer numerical control (CNC) milling, electrical discharge machining (EDM), LIGA process, micro-embossing and molding, electroforming, selective laser melting (SLM), electron beam melting (EBM), and additive manufacturing (3D printing) methods. These methods will be evaluated together with their field of application, superiorities, limitations, and technical difficulties.

1.2.1. Conventional Methods

These methods have limited capability to form micro patterns, but they improve the microstructural properties and surface integrity of the materials produced, which provides indirect advantages at the micro level.

1.2.1.1. Vacuum Melting and Remelting (VIM, VAR, ESR)

Superalloys and reactive metals, such as titanium (Ti), used in advanced technologies like jet engines and nuclear reactors, failed to deliver the desired performance when produced with traditional casting and melting methods (Sung & Kim, 2007). Then, the techniques for conducting melting under vacuum were developed in the 1950s (‘Vacuum Induction Melting Technology’, 1987). Vacuum induction melting (VIM) is a process that involves melting metal via inductive heating under a vacuum. It has been possible to melt the

superalloys without oxidizing niobium (Nb), aluminum (Al), and titanium (Ti) present inside, and to remove gases such as oxygen (O_2) and nitrogen (N_2) from the environment using this method (Choudhury, 1992). A significant increase in the performance and lifespan of turbine blades in jet engines has been achieved with VIM, resulting in considerable progress in aviation. The main advantages of VIM are the removal of gases, controlled chemistry through the addition of reactive metals into the structure, and slag-free production ('Vacuum Induction Melting Technology', 1987). The metals produced by VIM have a homogeneous microstructure. However, the process takes place in a vacuum environment, which results in high equipment and maintenance costs (Zanner, 2004). The residuals from the ceramic pots used may be incorporated into the metal structure, resulting in inclusions within the metal microstructure, which can cause a loss of strength and an increase in brittleness (L. Zhang et al., 2024).

Vacuum arc remelting (VAR) is a process of remelting a metal ingot prepared by VIM under vacuum in an arc furnace and then solidifying it from bottom to top (Campbell, 2023). It is generally applied before forging. Segregation, also known as nonuniform chemical composition of an alloy during solidification, is reduced by the movement of the melting/solidifying front throughout the metal pool (Williamson et al., 1997), while the removal of impurities like sulfur and oxygen can be managed by vacuum systems. In this way, the material to be machined at the micro level gains an isotropic matrix. However, the VAR process is energy-intensive and time-consuming due to low manufacturing speeds, which makes it costly.

Another melting method is electroslag remelting (ESR). A controlled electrode melts the metal in a slag pool, and the metal is re-solidified at the bottom (Campbell, 2023). Slag reacts with the metal and absorbs impurities, such as sulfur, keeping the alloy pure. ESR aims to obtain the same level of purity without the use of a vacuum system. ESR has superiority in terms of low costs compared to VAR. However, the chemical composition of the metal can be adversely affected, and process control can be complex if the slag is not selected appropriately (Schneider et al., 2023).

Metals whose defects are minimized at the micro scale can be obtained by double (VAR + ESR) or triple (VIM + VAR + ESR) melting techniques (Moyer et al., 1998). These materials have a higher chance of demonstrating success in micromachining because they provide a homogeneous matrix with the utmost available purity. As stated previously, VIM, VAR, and ESR methods contribute indirectly to micro-pattern formation.

1.2.1.2. Hot Working Processes

Metal forming is one of the oldest manufacturing processes. Bulk forming consists of forging, rolling, drawing, and extrusion, where considerable compressive strain is applied to yield better mechanical properties (Sharath, 2021). On the other hand, sheet forming encompasses the application of tensile stresses (Sharath, 2021). Here, heat-treated bulk forming techniques will be explained. In the forging process, impact or pressure is applied to give the metal the desired shape. The indirect contribution of the forging to the micro scale surface structuring is related to its improving effect on the microstructure of materials (Khodabandeh et al., 2005). Dendrites, which are multibranched crystals formed during solidification (Hogan, 2001), along with segregation and voids observed in metals produced by casting, can either be fragmented or joined together during forging. Metal grains are elongated in the direction of deformation, resulting in the formation of grain flow, also known as fibering (Suris et al., 2023). Thus, forged objects have a much more homogeneous and refined microstructure compared to cast objects (Suris et al., 2023). The inclusion defects are decreased, porosity is substantially eliminated, and smaller grain sizes are obtained, leading to an improvement in mechanical properties. The drawback of forging is that it is incapable of forming complex shapes in unfilled parts.

Another method is hot rolling, where the metal is passed between rolling cylinders, thinned, and shaped (Ikumapayi et al., 2020). Hot rolling is the fundamental method for converting metal ingots into thin sheets and plates, and it is highly efficient in eliminating the heterogeneity resulting from casting (Ikumapayi et al., 2020). The hot-rolled metals develop an equiaxial grain structure with smaller grains due to recrystallization, and the voids from the casting are mainly confined (Shen et al., 2016; Uan & Cheng, 2007). In terms of surface structuring at the micro level, the hot rolling provides a high-quality surface and microstructure. However, the rolling produces linear or simple curved forms, so it cannot create patterns on the surface freely. Thus, one should use other techniques, such as photolithography, if micro patterns are desired on the metal surface.

The other hot-working technique is extrusion, where metal is softened by heat and pushed through a die to form a continuous profile (Yadav et al., 2018). It is commonly used for ductile metals, like aluminum and copper, to produce rods and pipes. Metals produced through extrusion are subjected to high plastic deformation, which eliminates segregations and voids that occur during casting (Leśniak et al., 2024). Additionally,

grains are elongated in the direction of flow, and smaller grains are formed through recrystallization (Leśniak et al., 2024). The wires and rods with smaller diameters (smaller than millimeter level) can be produced by extrusion or can be cut to be converted to micro components. For example, thin copper wires used in electronics are obtained through the extrusion process (Li et al., 2021). The advantage of extrusion is that it produces complex cross-sectioned materials in a single step. However, it requires high forces and specialized molds, and the size of the product is limited to the die opening, which makes the extrusion disadvantageous.

In summary, forging, hot rolling, and extrusion, which are primarily volume-based shaping processes, cannot directly contribute to micro-scale surface texturing; however, they provide significant improvements in the microstructure of the materials and pave the way for micro-manufacturing.

1.2.1.3. Hot Isostatic Pressing (HIP)

Hot isostatic pressing is a method developed to eliminate internal porosity in metals and achieve the fully dense form of materials. Porosity, especially in metals, is a critical defect that affects fatigue and strength, and has a more substantial impact than defects in the microstructure (Antona & Mapelli, 2001). In the HIP process, the material is exposed to high temperatures (generally over 1000°C depending on the material) and high pressures (commonly over 98 MPa) in all directions (isostatic) (Bocanegra-Bernal, 2004). For high pressures, Argon gas is used mainly at around 100 MPa or higher. Under these circumstances, the voids in the material itself are confined by plastic deformation, creep, and diffusion, and microporosities are collapsed, thereby increasing the density of the material. At the end of HIP processing, fractures that internal defects may cause are eliminated, and the fatigue life and toughness of the metals are significantly improved (Atkinson & Davies, 2000). From the perspective of micro-scale surface structuring, HIP eliminates porosities resulting from the production process and achieves full density, even in regions close to the surface. Additionally, the phases within the material can be distributed homogeneously due to exposure to high temperatures over extended periods. The disadvantages of HIP process are that it requires high-pressure furnaces, prolonged times, and is costly due to its energy-intensive nature; also, the size of the parts is limited to the press chamber (Herrmann & Räthel, 2021). Nevertheless, it has been utilized in

several critical applications today, such as turbine discs and medical implants, and has become a standardized final process. It is used for metal parts that require reliability at micro scale to increase quality.

To sum up, conventional methods underlie micro manufacturing by improving the microstructure, purity, and density of the material, even though they are not used directly to form features on the surface at the micro scale.

1.2.2. Modern Techniques

The surface structuring at the microscale has been made possible with advanced manufacturing technologies. Some of these methods are adapted from the semiconductor industry, such as photolithography and lithography-based techniques. Others are mechanical micro bench techniques that rely on subtractive manufacturing or scaled-down versions of the existing manufacturing methods. Another technique is additive manufacturing (3D printing).

1.2.2.1. Photolithography

Photolithography is one of the earliest micro-manufacturing techniques. Historically, photolithography has been used in the production of electronic chips and has become revolutionary due to its capacity to transform micro patterns on a large surface. In general terms, the technique is based on reflecting UV light onto a photoresist plate with the aid of a mask, followed by the dissolution of the photoresist in the desired pattern as presented in Figure 1.6 (Pimpin & Srituravanich, 2011). Although photolithography was first developed to pattern circuits on silicon semiconductor wafers, it has also been used to shape metal surfaces at the micro scale. For example, to utilize thin metal films made from copper or gold as conductive paths in microelectronics or sensors, photolithography is applied to them. A metal film, approximately 1–2 micrometers in thickness, covered on a ceramic base, can be carved using chemical etching with the creation of a mask in the desired geometry through lithography. This approach is like a micro version of photolithographic etching in printed circuit boards (PCBs). The most advantageous part

of photolithography in micro scale surface structuring is its high sensitivity and compatibility with massive production.

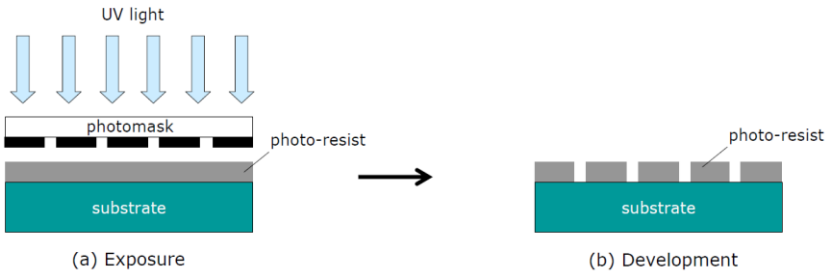

Figure 1.6. (a) Exposure to UV light on a photoresist coated substrate, (b) Development of the pattern (Pimpin & Srituravanich, 2011)

Many parts on a wafer can be patterned at resolutions below the micro level using a single mask. Photolithography is limited to optical resolution, which is known as the Abbe-Rayleigh diffraction limit (Ito & Okazaki, 2000). This limit is determined by the wavelength of the incident light and the numerical aperture of the system. Photolithography has several drawbacks. First, it defines only planar geometries, or 2D, as the mask is applied perpendicularly (Tam-Chang & Iverson, 1999). The height of the micro pattern relies on the covering and carving processes but is ultimately limited by the thickness of the photoresist. It is therefore challenging to construct structures that possess a high aspect ratio (height:width). A 10 µm wide, 500 µm high column cannot be achieved by photolithography alone. This limitation is addressed by the LIGA process. Additionally, photolithography requires integration with other etching or deposition methods, making it a multi-step process. Additionally, the process requires a cleanroom (Tam-Chang & Iverson, 1999). Nevertheless, it can be regarded as the first micro-machining technique in history and remains an essential method in electronics and sensor applications.

1.2.2.2. LIGA Process

LIGA stands for Lithographie, Galvanoformung, Abformung in German, which translates to lithography, electrodeposition, and molding, respectively (J. H. Kim et al., 2014). It utilizes the high sensitivity of photolithography to produce microstructures with high

aspect ratios. In this process, a very thick, in the order of millimeters, light-sensitive polymer plate, such as polymethyl methacrylate (PMMA), is masked by X-ray lithography, deep perpendicular voids are created, and the voids are finally filled with metal (Malek & Saile, 2004). To be more specific, a few hundred microns-thick photoresist plate, such as PMMA, is attached to a conductive plate. X-rays sourced from a synchrotron are passed through an X-ray resistive metal mask. X-rays can penetrate more deeply compared to UV and pass through the photoresist. Depending on the photoresist material, either the irradiated or the unirradiated regions are dissolved, creating deep molds. These hollows are filled with metal ions through electrodeposition, using the bottom conductive plate as an electrode. Metal ions accumulate inside the cavities and solidify, taking the shape of the entire cavity. The rest of the photoresist plate is dissolved completely by chemical methods, and the metals grown inside the cavities are brought out. These metal structures can be used either as the end product or as a mold insert. The most important result of the LIGA process is that it can produce microstructures with high aspect ratios as illustrated in Figure 1.7 (Hormes et al., 2003).

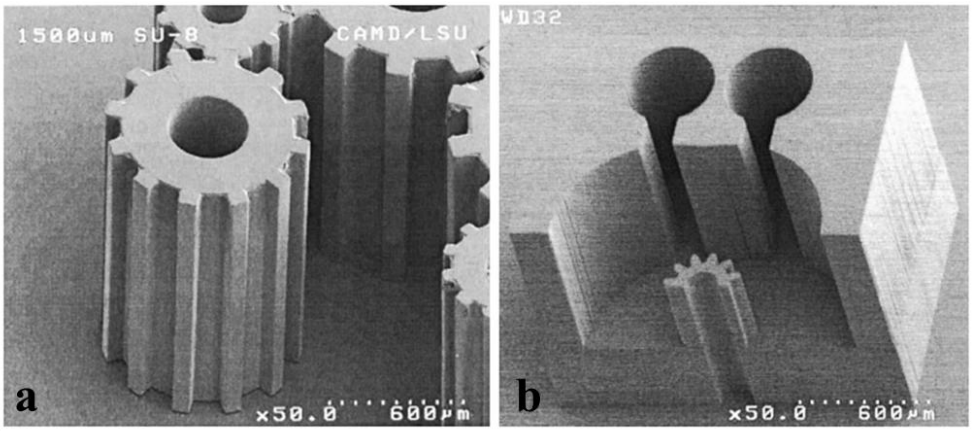

Figure 1.7 (a) Gears with 1500 μm height, (b) Three level structure with step heights of 300, 600 and 900 μm (Hormes et al., 2003)

Additionally, the objects obtained through the LIGA process have sharp edges with a resolution of less than 1 μm due to the parallel X-rays generated by the synchrotron. The major drawback of the LIGA process is its reliance on a synchrotron, which renders the process dependent on an extremely expensive and limited facility (Hahn et al., 2005). Another disadvantage of the LIGA process is its inability to produce patterns in multiple dimensions. Hence, if patterns with different heights are desired on a part, the process

needs more than one LIGA process to be applied. Moreover, the electrodeposition step is too slow, so forming nickel coatings with a thickness of 100 μm takes hours and even days. The LIGA process is primarily used in micro-optic components, micro-gears, motor components, micro-needles, and micro-electromechanical systems (MEMs) (Hruby, 2001). Nowadays, LIGA still finds its place in applications, but it remains in the realm of special industrial needs and research scales due to the need for a synchrotron facility.

1.2.2.3. Micro CNC and Electrical Discharge Machining (EDM)

CNC benches and electrical discharge machining (EDM) systems can produce features at the micro scale after advancements in optics and the mold industry. Today, the positioning sensitivity of CNC benches has been improved by laser interferometer measuring systems. Additionally, micro-turning, milling, and drilling processes can be operated with cutting tools having diameters of less than 50 micrometers. In micro milling, carbide mills with diameters of 50 μm or 100 μm are used to create pockets or channels in metals such as steel, aluminum, and copper. Micro turning eliminates the surface roughness in the order of one thousandth of a millimeter. For example, brass parts of micro connectors used to connect optic fibers are processed by micro turning, and the roughness can be eliminated up to the quality of a mirror. The advantage of CNC machining is the ability to create flexible geometry (Newman et al., 2008). In other words, the design flexibility is higher than the many methods; three-dimensional bodies, complex pocket structures, or angular surfaces can be machined. Moreover, it can be applied to different metals. However, it has tool limitations. Tools at the micrometer level are highly delicate and can be easily broken, and these tools can only work at shallow depths. The bench costs are high due to the high spin and sensitive tool holder requirements. In addition to these drawbacks, each piece of material can be machined individually, despite the complete automation, which makes it slow for mass production. In micro milling, the placement of the small piece to be machined, its stability during machining, and the circumvention of vibration are critical issues to consider. Nevertheless, micro CNC is an irreplaceable tool in the prototyping and manufacturing of micro molds.

Electrical discharge machining (EDM) is a commonly used method for creating complex shapes on hard and difficult to machine materials at the macro level. Micro EDM is the application of this technique, utilizing microelectrodes and sensitive positioning.

Principally, it works only on conductive materials such as metals and conductive ceramics. Micro EDM has two types (Mahendran et al., 2010): sinker EDM and wire EDM. In sinker EDM, a shaped graphite or copper electrode is immersed, along with the workpiece, in dielectric fluid. The mirror image of the electrode is transferred to the workpiece. On the other hand, a thin wire, generally made from brass, is used as an electrode for wire EDM, as its name implies. The wire moves through the part to be shaped and sparks as it moves to remove the material. The most advantageous aspect of EDM is its non-contact machining method (Ho & Newman, 2003), which eliminates the need for cutting or drilling forces, making the machining process applicable to brittle or very hard materials at the micro scale. Another advantage of EDM is that it provides high-dimensional resolution on the order of ±1 μm. Microcavities created by EDM are presented in Figure 1.8 (Yan & Lin, 2011).

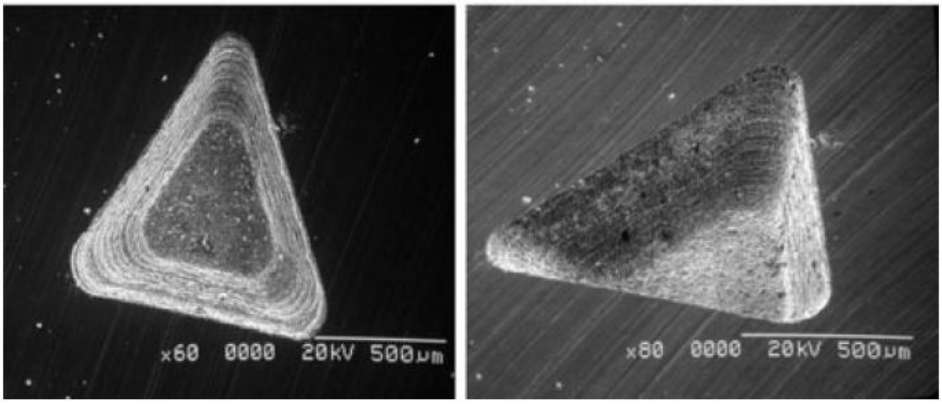

Figure 1.8. Microcavities created by EDM (Yan & Lin, 2011)

However, EDM has disadvantages: it can be applied only to conductive materials (Ramasawmy & Blunt, 2004), its machining speed is too low, and it can cause thermal damage to the surface since the electrical arc erodes the material (Max, 2025). Even though the discharging energies are kept low, additional polishing steps might be required to obtain a defect-free surface. Another drawback of EDM is that it is difficult to produce complex 3D forms (Y. Liu et al., 2023). Since EDM typically constructs the negative of the mold, geometries with convex and concave structures require multiple-axis scanning, which can be laborious at the micro scale. Today, micro EDM is used industrially in micro hole drilling applications such as cooling holes in turbine blades in aviation, fuel nozzle holes in diesel injectors, and side holes in medical needles.

1.2.2.4. Micro Forming

Micro forming refers to the production of small pieces, whose at least two dimensions are smaller than 1 millimeter (Zimniak, 2020), through plastic deformation methods. It has subdivisions: micro forging, micro extrusion, and micro sheet forming. With these methods, whose equivalents at the macro scale have already been efficient, the mass production of small parts can be possible. Indeed, the need for metal pieces smaller than millimeter sizes has been increasing in the fields of electronics, telecommunications, and medicine, and it has been a final goal to obtain thousands of these economically. The advantages of the micro forming are high productivity and material efficiency. Since it does not remove material, as in the case of machining, the material waste is very low. Once a suitable mold has been prepared, cycle periods are substantially shortened. However, it encounters problems (Geiger et al., 2001) regarding the dimension. The most critical issue is the scaling effect. The flow behavior of the material depends on the particle size. As the thickness to grain size ratio gets lowered, flow is determined by the grain behavior. Moreover, friction between the mold and the workpiece increases proportionally as the workpiece becomes smaller, because the area to volume ratio becomes higher. Another problem is the sensitivity of tools and equipment. Since the dimensions are small, the workpiece can be defective rather than controlled plastic deformation. Despite all these difficulties, micro forming leads to successful industrial products, such as screws in smartphones or medical stents, and micro surgical device parts (Geiger et al., 2001; Sharma et al., 2022). Figure 1.9 presents the ossicle implant produced via microforming

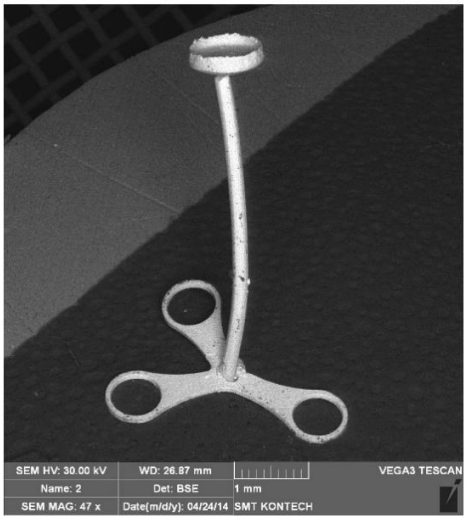

Figure 1.9. The ossicle implant produced via microforming (Zimniak, 2020)

1.2.2.5. Electroforming

Electroforming is a method to construct an object by accumulating metal. Its working principle is based on electroplating, but the difference between them is that electroforming creates entirely new objects rather than improving existing ones (MacGeough et al., 2001). Electroforming is an attractive method due to its ability to produce precise copies. The technique (H. Zhang et al., 2020) requires a master mold, also known as a mandrel. The mandrel is immersed in an electrolyte solution and serves as the cathode. The anode, on the other hand, is typically a soluble metal, such as copper or nickel. When the current is applied, metal ions begin to deposit on the mandrel, and the process continues until the desired thickness is reached. Then, the metal covering the mandrel is carefully removed, and some agents may be used to facilitate the removal of the metal from the mandrel. In this way, the pattern on the mandrel surface is impressed on the inner side of the metal, so the metal bears the negative of the mandrel. A micromesh nickel screen produced via electroforming is shown in Figure 1.10 (Ming et al., 2010).

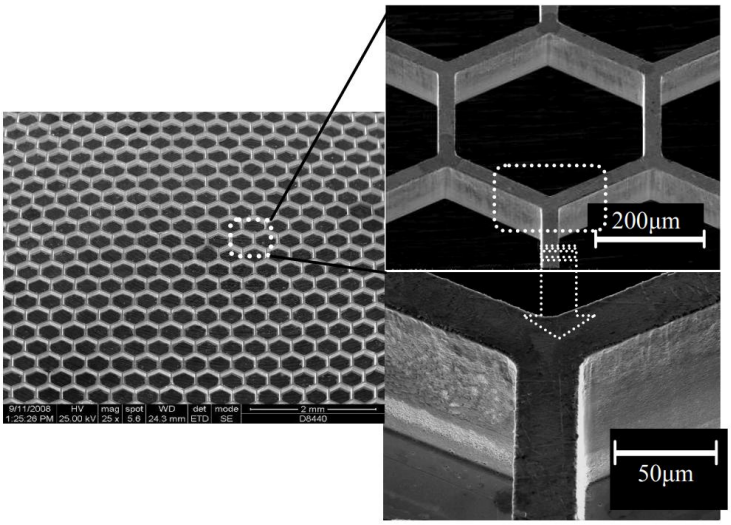

Figure 1.10. A micromesh nickel screen produced via electroforming (Ming et al., 2010)

The advantage of electroforming is that it allows for the precise reproduction of complex and delicate micro details. Once the master mold is available, electroforming can produce the exact metal copies of it. The process takes place at room temperature, so there is no thermal deformation or change in microstructure. However, the technique is dependent on the preparation of the mold (Sole, 1994), meaning a master mold should be produced with a different method to create an object from scratch. Electroforming alone does not

provide design freedom; it only produces replicas. Secondly, it is a slow processing technique with low volume efficiency, meaning that making a thick and big object can take months. Thirdly, there is material limitation. The best performing metals in practice are nickel and copper (MacGeough et al., 2001; Sole, 1994), which can be electrodeposited via aqueous solution. While electroforming is primarily used for mold production purposes, microfilters, sieves, and porous structures can also be electroformed for use in blood filtration or fuel cell plate applications.

1.2.2.6. Selective Laser Melting (SLM)

With the advancements in additive manufacturing technologies, it has been possible to form layer by layer structures of metals by melting their powder form with a laser or electron beams. Selective laser melting (SLM) is also known as laser powder bed fusion (LPBF), is one such technique. In SLM, a thin layer of metal powder is spread, and a laser beam melts the desired section, and then a new layer of metal powder is spread again onto the melt (Leitz et al., 2017). This process is repeated several times until a 3D object is obtained (J. Zhang et al., 2019). Figure 1.11 presents the schematic of the process and machine parts made from Molybdenum by SLM (Leitz et al., 2017). This technology has revolutionized manufacturing owing to its capability to produce without a need for a mold. From the perspective of surface structuring at the microscale, the innovation introduced by SLM enables the production of intricate inner constructions and surface details monolithically. For example, if a network of zig-zag-like microchannels or lattice structures is desired inside a metal part, it can be produced by SLM at one time. In contrast, it would require multiple steps or be impossible to produce using previous methods. The advantages of SLM can be listed as follows: design flexibility, eliminating the need for a mold or tool, monolithic production, and rapid prototyping, which shortens the time for product development (Manakari et al., 2016). On the other hand, it has disadvantages, including high surface roughness of around 10 μm Ra (roughness average), a lengthy processing time that depends on the object's size, high costs due to metal powders and equipment, and the fact that it is an energy-intensive process. It also requires special equipment for powder handling and is not suitable for all metals, particularly those with higher thermal conductivity, like copper, which reflects the laser. There has been ongoing research to improve the surface roughness, to form composite

structures by providing different metal powders at the same time, and to speed up the process with multiple use of lasers.

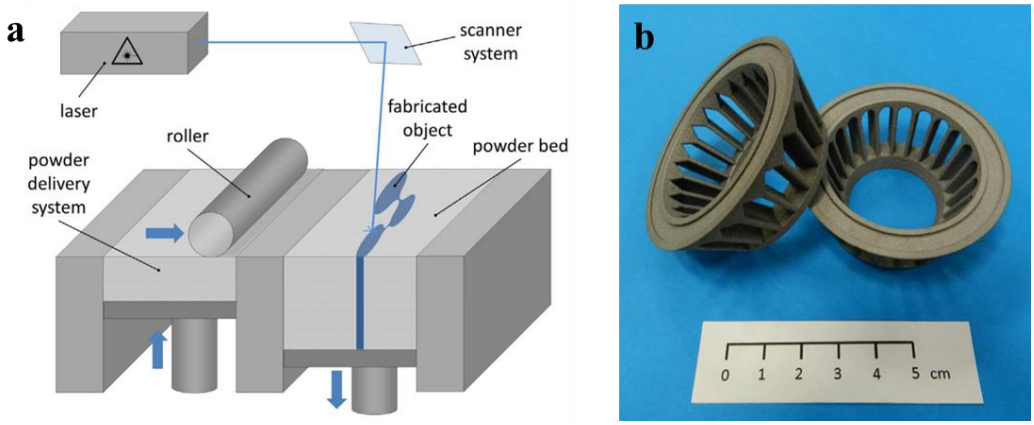

Figure 1.11. (a) SLM process, (b) Machine parts made from Molybdenum by SLM (Leitz et al., 2017)

1.2.2.7. Electron Beam Melting (EBM)

Electron beam melting (EBM) is another powder bed fusion technique that works with similar principles to SLM (Gokuldoss et al., 2017). As the name implies, the electron beam is used for melting in EBM rather than a laser. The process must take place in a vacuum environment because electrons cannot move in the air. Also, a vacuum environment is needed to prevent oxidation at high temperatures. EBM is preferred, especially for refractive materials or titanium containing alloys, because lasers cannot reach the temperatures that EBM can reach as efficiently as EBM. Compared to SLM, the electron beam in EBM can be moved fast with the use of electromagnetic lenses. That's why EBM can melt powder more quickly by reducing production time. Additionally, the electron beam can scan the powder for pre-heating before melting, ensuring that each layer remains hot and eliminating tensions resulting from temperature differences. However, the process is expensive owing to the vacuum requirements. The size of the object that EBM can produce is limited to the size of the vacuum chamber. The electron beam cannot be focused as much as a laser, and therefore, surface roughness is higher compared to SLM. The range of materials that can be used is narrower than that of SLM. Stainless steel and aluminum are not utilized in EBM because aluminum can easily

vaporize in a vacuum, while stainless steel may lead to problems related to magnetism. While EBM is not as popular as SLM, it is preferred for its fast processing in production of large parts.

1.2.2.8. Binder Jetting

Binder jetting is another additive manufacturing technique that involves spraying a liquid binder into a powder bed (Dini et al., 2020). In this method, a head similar to an inkjet printer head sprays the binder droplets after a thin layer of powder is spread. The sprayed binder joins the powder particles together in that layer. After completing each layer, the platform is lowered, and a new layer of powder is spread onto it. Then, the binder is resprayed. This process is repeated until the object, called the green body, is constructed. At the final step, the green body is removed from the powder bed, and the excess powder surrounding the object is cleaned. The green body is then heated for binder curing. To achieve high density, the green body is sintered. It offers design flexibility and is compatible with various materials. The binder spraying takes place at room temperature, and distortions resulting from the melting by laser or electron beam are eliminated. Its green body production time is high because it can print the surface of the entire layer simultaneously, and the cost per material is low. Since the powder bed supports the object in construction, complex shaped objects or objects with hollowed structures can be produced without the need for support. However, the process has drawbacks (Gibson et al., 2021). The green form of the objects has high porosity and is relatively weak. Even after sintering, the objects can have a lower density and strength compared to those produced by fully melting techniques. The printed objects are not ready for direct use in their intended application. It requires several post-processing steps, including curing the binder, removing excess powder, and sintering. This makes the entire process time-consuming, and each step might cause dimensional changes, which in turn makes control of tolerance difficult. The green body can be easily damaged when it is removed from the powder bed or during the sintering process. The binder jetting process is used in the prototyping of complex metal components in the automotive and aviation industries.

1.2.2.9. Directed Energy Deposition (DED)

Directed energy deposition (DED) is based on the principle of melting metal using a focused energy source, such as a laser, electron beam, or arc plasma. In this method (Svetlizky et al., 2021), metal, in the form of powder or wire, is fed into the melt pool, where it is fused with the bottom surface. For the laser DED systems, powder feeding is used. The nozzle blows the metal powder to the point where the laser melts it. Hence, material is deposited as a line by forming a welding seam. In the case of wire feeding DED, the arc or electron beam melts the tip of the wire and the melted wire is deposited at the bottom. DED processing is operated with 4- or 5-axis automated head, which provides the addition of material to the different regions at various angles. Either the completely new component is placed onto a substrate by an additive method, or it can be added to an existing surface for repair or coating purposes. After each layer, the head changes its position to build another layer. DED can be viewed as an automated welding process, where the material solidifies rapidly at the moment of melting, and the processing point moves continuously to create a 3D structure. It is highly efficient in the production of large pieces with 5 kg/h deposition speeds. While the size of the structure in SLM is limited by the size of the powder bed, the nozzle in DED can move automatically to produce parts in meters or add to an existing large piece. This makes DED advantageous, especially in aerospace and aviation, for large single-piece components or thick-sectioned pieces. The materials that can be used are varied due to two feeding options: powder or wire. Moreover, the feeding material can be changed during the processing, and alloy transitions in the material can be formed, which makes DED unique in designing new alloy types. However, the material traces are thick, in the order of millimeters, which results in rough surfaces in the constructed materials, and the pieces may require additional processes to achieve smooth surfaces (Svetlizky et al., 2021). The objects produced with this method cannot have as sharp edges as, nor as thin walls as, the objects created by SLM. Since the DED process is a welding process, the piece is continuously exposed to high temperatures, which may cause distortions, unwanted microstructures, and phase formations. It isn't easy to control the cooling of the object in the DED process. Finally, DED benches are costly due to complex equipment requirements, including multiple-axis automated systems, focused high-energy sources, and sensitive powder feeding nozzles. Although it offers low manufacturing costs for large pieces, it is not economical for the small pieces. DED technology is primarily used in the manufacturing

of large components, such as large fuel tanks for rocket and space applications, or propelling motor bodies, as well as in their repair and coating applications.

In conclusion, the surface structuring of metals represents a technological transformation from the past to the present. The conventional metallurgical and manufacturing methods, from vacuum melting to hot isostatic pressing, pave the way to the present micro manufacturing by improving the microstructure and purity of the material. These homogenous and small grain sized metals obtained from conventional methods present successful results in the micro machining steps applied later. Meanwhile, modern techniques, starting with photolithography and developed through LIGA, micromachining, EDM, electroforming, and ultimately culminating in additive manufacturing methods, can be seen as a series of methods. Each method at the micro scale has its own contributions and limitations, and the development of surface structuring techniques is directed by the needs. While further advancements make it possible to access smaller, lighter, and smarter technologies, they also present challenges in engineering skills needed to push the limits of materials and complex geometries.

CHAPTER 2

2. MATERIALS AND METHODS

2.1. Materials

Inconel 718 powder was purchased from MSE Supplies and used directly without additional treatment. Three polyvinyl alcohol (PVA) polymers with different molecular weights, supplied by Aldrich, were tested as binders. The crystalline form of the PVAs was dissolved in deionized (DI) water at 80°C for approximately 2.5 hours, depending on the molecular weight of PVA, to obtain a 5% (w/v) solution. The PVAs were labeled according to their molecular weights and tabulated in Table 2.1.

Table 2.1. Properties of supplied PVAs

Label	**PVA-1**	**PVA-2**	**PVA-3**
Molecular Weight (Mw) [g/mol]	9,000–10,000	13,000–23,000	85,000–146,000
% Hydrolyzed	80%	87-89%	87-89%
Form	Crystals	Crystalline powder	Crystals
Product Code of the Supplier	1002455665 **360627-500G**	101926148 **363170-500G**	**36308-1**

DI water was sourced from a Millipore Milli-Q Reference Ultrapure Water System, and its resistivity was reported as 18.2 MΩcm, which was used in the preparation of all metallic doughs and the PVA solutions.

2.2. Preparation of the Green Bodies

The metal powder is weighed into a beaker so that the solid loading is greater than 90 wt%. Since the purpose is to prepare the metallic doughs with the highest possible solid loading while keeping the binder percentage with respect to the metal powder as low as possible, the metallic doughs can be obtained with less than 0.15 wt% binder. The binder weight percentages are given in relation to the amount of metal powder in the dough. The remaining formulation consists of DI water, which serves as a dispersing medium for the water-soluble binder, while minimizing the chemical amount for sustainability considerations. To determine the amount of binder solution to be added to the dough, the solid content of the binder was measured using a SHIMADZU MOC63u. Although the binder solution is prepared to obtain a 5% (w/v) concentration, the solid content analysis reports the actual percentage of PVA in DI water as 4.95% in the prepared solution. The amounts of the materials are determined by the weight percentages in the formulation, which is 94.5% solid loading and 0.13% aqueous PVA-3 relative to metal powder. To prepare the dough, the metal powder was weighed into a beaker first. The binder solution was added to the DI water. Since the amounts are too small to handle, the mixture was taken and released several times by the micropipette to ensure a homogeneous mix. Then, this mixture was added dropwise to the metal powder while mixing with a spatula by hand. The uniform distribution of the binder to cover the metal particles and to connect bridges among them was ensured by the synchronous dropwise addition of the binder and vigorous mixing for approximately 1.5 minutes. At the end of this process, the metallic dough was ready and could be either surface structured or molded. This form of the dough is called green body.

2.3. Surface Structuring and Molding

2.3.2. Surface Structuring by 3D Printed Objects

Patterning wheels, stamps, rollers, and pyramids to texture the surface of metallic doughs were manufactured at Sabanci University, CoSpace through 3D printing (Figure 2.1). Ender 5 S1 3D printer was used with Polima PLA filament to obtain 3D printed objects.

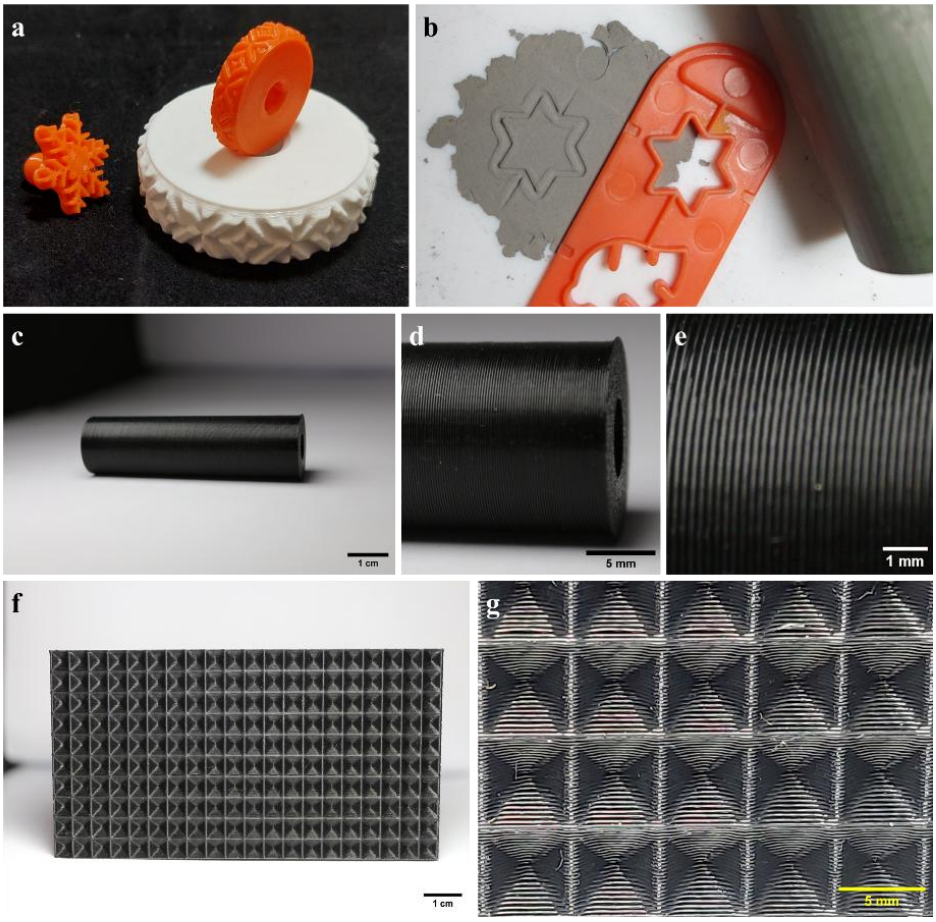

Figure 2.1. 3D printed (a) Snowflake stamp and patterning wheels, (c-e) roller and its magnified images, (f-g) pyramid stamp and its magnified image. (b) Star stamp, it is not 3D printed, but used for surface structuring

Upon preparation in a beaker, a spherical shape was induced by hand and the dough was placed onto a flat surface. A rolling cylinder was used to spread the dough onto the surface. Then, the surface of the dough was shaped by stamps, wheels, or rollers. The spacing of the lines for the roller (Figure 2.1. c-e) was measured as 200 µm by using ImageJ software.

2.3.3. Molding

The cylindrical and prismatic molds with specific dimensions were obtained by engraving plexiglass with a laser cutter at Sabancı University, Co-Space. The laser cutter has a power of 300W and a working area of 130 cm x 90 cm. Some of the molds and the laser cutter are provided in Figure 2.2.

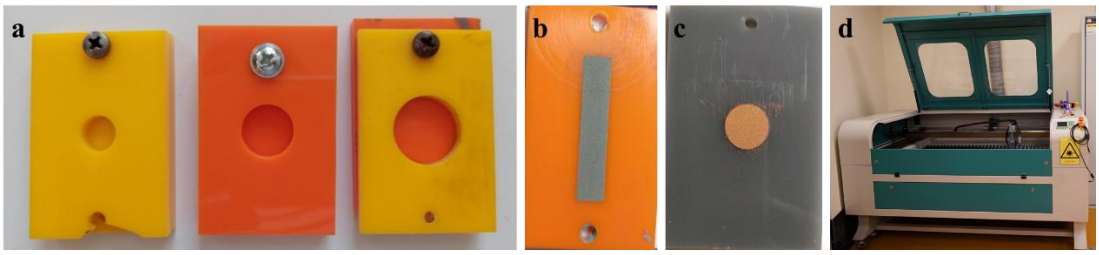

Figure 2.2. (a) Cylindrical molds of various sizes, (b) Prismatic mold into which Inconel 718 dough was filled. (c) Cylindrical mold into which Copper dough was filled. (d) Laser cutter at Sabancı University, Co-Space

When the dough was prepared, it was removed from the beaker and pushed into the mold. A spatula was used to smooth the surface and press the dough further, ensuring that no air was trapped between subsequent additions of the dough. This process was repeated until the mold was filled. The excess dough was taken from the surface with the help of a stamp whose base is made from perfectly flat plexiglass. After completion of the front side, the same process was repeated for the back side of the mold. In this way, it was assured that the mold was filled with no voids, and the dough acquired the exact shape of the mold. The dough can be removed from the mold by uniformly applying pressure with an object of similar size, ensuring that the front side of the dough remains undamaged and no pieces of dough are left in the mold.

2.4. Sintering Profile

Sintering is a thermal process in which atomic diffusion occurs to strengthen the material by enhancing densification. Several sintering profiles, as shown in Figure 2.3, were tested for Inconel 718 prepared with PVA-3 to achieve optimal mechanical properties. Argon (Ar) gas (UN 1006) was introduced to prevent oxidation of the samples when tube furnaces were utilized. The profile presented in Figure 2.3.d was taken from the study of Paul (Paul, 2022).

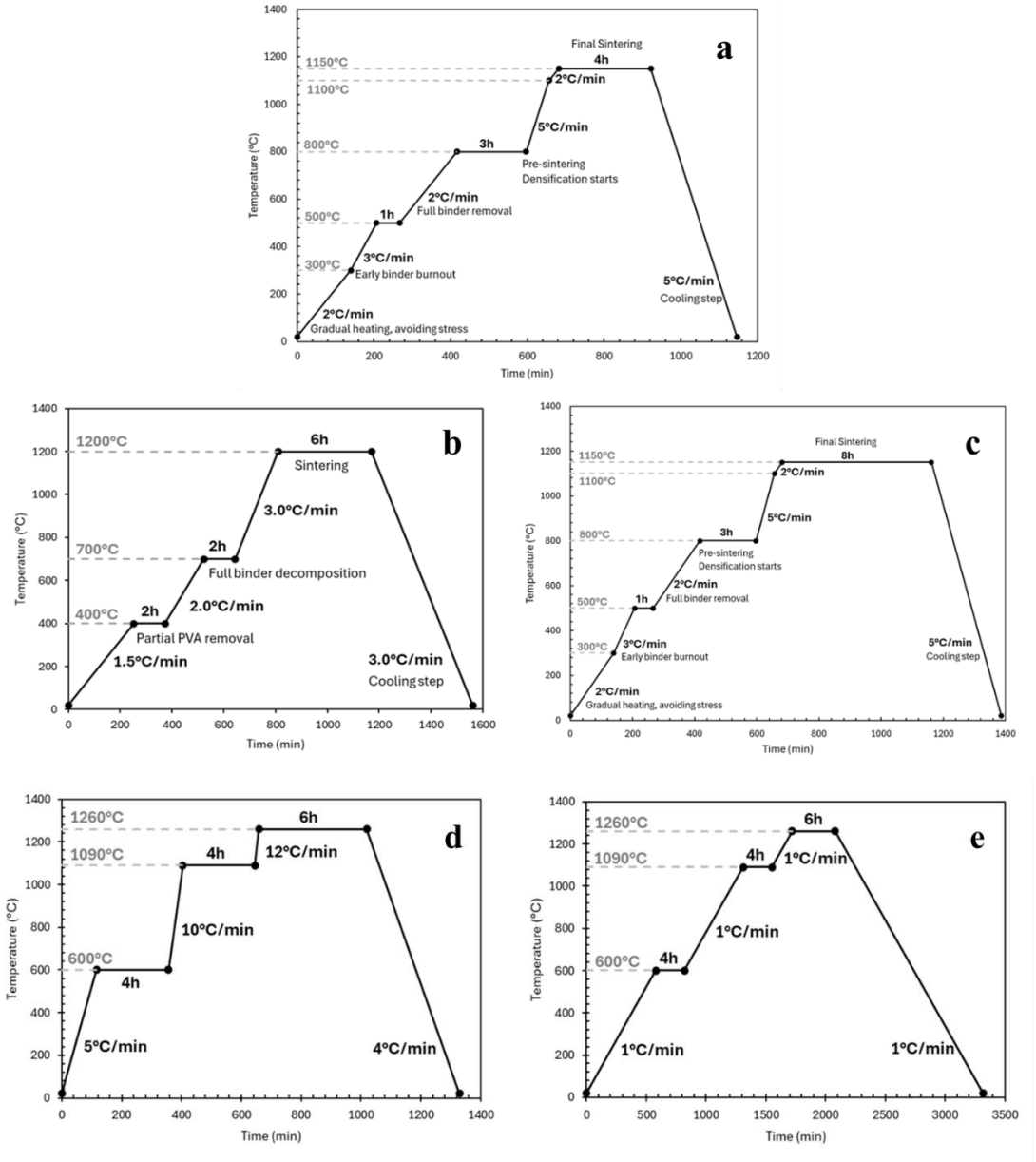

Figure 2.3. (a and c) PROTHERM PTF 12/50/450 tube furnace under 200 cc/min Argon flow, (b) PROTHERM MoS-B 180/4 chamber (box) furnace under an air atmosphere, (d), and (e) PROTHERM PTF 14/75/450 tube furnace under 3l/min Argon flow.

Initially, there was no flowmeter in use; therefore, the Argon flow was adjusted solely by setting the regulator pressure to a minimum value of less than 0.1 bar. Later, a Dwyer Instruments RMA-11-SSV flowmeter, which has a maximum flow capacity of 200 cc/min, was connected to enable controllable adjustment of the Argon flow while using the PROTHERM PTF 12/50/450 tube furnace.

To work at higher temperatures, we used (Figure 2.3 e and f) a PROTHERM PTF 14/75/450 tube furnace capable of reaching a maximum temperature of 1400°C. The

pressure regulator of the Argon cylinder used with this furnace has its own attached Argon flowmeter.

2.5. Characterization of Metal Powder, Green Bodies, and Sintered Bodies

This section outlines the characterizations performed on the metal powders, as well as the green and sintered bodies.

2.5.1. Particle Size Analysis (PSA)

PSA on Inconel 718 neat powder suspended in DI water at three different concentrations was conducted using a Malvern Mastersizer 3000E. The prepared solution was added to the Hydro SM device until an obscuration of 5% was achieved. The analysis was also performed with the same concentrations, but with the addition of 0.13 wt% PVA-3 with respect to the metal powder, which is the optimum percentage in Inconel 718 dough when PVA-3 is used as a binder. The objective is to examine the effect of the PVA-3 on Inconel 718 metal powder particles by comparing the results with those of neat Inconel 718 powder. The particle refractive index and absorption index for Inconel 718 are 1.96 and 4.00, respectively. The water acts as a dispersant, and its refractive index is 1.33.

2.5.2. Rheological Behavior of Doughs

An Anton-Paar MCR92 rheometer was used to investigate the rheological properties of Inconel 718 doughs prepared by PVA-1, PVA-2, and PVA-3. A parallel plate (PP) with a diameter of 25 mm was utilized. The analysis was conducted at room temperature (25°C). Immediately after the dough was prepared, it was manually shaped into a spherical form. The spherical dough was placed onto the flat base of the instrument. The gap size was set to 2-3 mm, depending on the dough size. Measurements were conducted using three distinct pieces of each dough. The shear rate was adjusted from 0.1 to 100 s^{-1} during flow curve measurements for viscosity determination. Amplitude sweep analysis was performed on each dough to observe how the storage (G') and loss (G'') moduli change

with the strain range of 0.01% to 100%, while keeping the angular frequency constant at 10 rad/s.

2.5.3. Determination of Density and Expansion

The volume measurement of the green and sintered bodies was conducted using a Micromeritics AccuPyc II 1340 with a 3.5 cm^3 cell and a steel volume reducer numbered 0, having a known volume of 1.53 cm^3. The volume reducer was used because the sample was too small for the cell. By adding the volume reducer, the chamber size was decreased, and pressure sensitivity was improved, also resulting in less utilization of He gas during the analysis. Before using the instrument for analysis, a calibration was required using a 3.5 cm^3 cell with its standard calibration ball. After the calibration, the instrument is ready. Thus, the Inconel 718 doughs with PVA-3 binder were prepared and molded using a mold with dimensions of 10.20 mm in diameter and 4.65 mm in height to create a standard shape, before measuring the volume. At first, the solid content of the dough was measured by using SHIMADZU MOC63u. Then, the cylindrically shaped dough was weighed. The dough was placed into the cell, and the analysis was started to measure the volume. The mass and the reported volume were used to calculate the density of the dough immediately after its preparation. The percentage of expansion and the change in density were determined after repeating the measurements on their sintered bodies.

2.5.4. Thermogravimetric Analysis (TGA)

TGA was conducted to ensure the removal of the binder from the dough during the sintering process. The analysis was performed on the crystalline form of PVA-3 as supplied, a 5% (w/v) aqueous solution of PVA-3, and an Inconel 718 dough with a PVA-3 binder. TGA was conducted using a NETZSCH STA 449C Jupiter instrument, where the temperature was ranged from 25°C to 1200°C at a heating rate of 10°C/min in a nitrogen atmosphere.

2.5.5. X-ray Diffraction Analysis (XRD)

XRD analysis was performed to reveal the crystalline forms and phases of the metals available in the structure. For this purpose, the Bruker D8 Advance instrument in SUNUM was used, with 2θ ranging from 5° to 90°. The voltage and the current of the X-Ray generator were set to 40 kV and 40 mA, respectively. Motorized primary divergence slit angle was adjusted to 0.18° and time was entered as 1 s. The analysis was performed on Inconel 718 metal powder, Inconel 718 dough with a PVA-3 binder, and sintered bodies of Inconel 718 prepared with a PVA-3 binder.

2.5.6. Mechanical Characterization

The bending stress of the sintered Inconel 718 prepared with PVA-3 was assessed using a Universal Testing Machine (UTM), which is Zwick/Roell Z010. The sintered sample dimensions were around 40 mm × 7.5 mm × 5.5 mm. The three-point bending configuration was used with a test speed of 0.5 mm/min. The test standard was chosen as ISO 7438 from testXpert II V3.6 software.

2.5.7. Scanning Electron Microscope (SEM) and Energy-Dispersive X-ray Spectroscopy (EDS)

SEM micrographs were captured to examine the surface texture formed on Inconel 718, prepared with PVA-3, before and after sintering at varying acceleration voltages of 5 to 15 kV. This observation aimed to determine whether the shape transfer from the stamps or rollers to the dough maintained the same fidelity. As the metal is conductive, a coating is not necessary. EDS analysis was also conducted on the same samples before and after sintering to assess the elemental composition. The JEOL JSM-6010 LV for SEM and OXFORD Instruments for EDS at SUNUM were used.

CHAPTER 3

3. RESULTS AND DISCUSSION

3.1. Formulation of Doughs

The three PVAs given in Table 2.1 were used to prepare aqueous solutions with 5% concentration and tested as binder solutions in the formulation of Inconel 718 dough. The solid loading weight percentages were 94.8%, 94.2%, and 94.5%, while the PVA weight percentages with respect to the metal powder were 0.15%, 0.15%, and 0.13%, respectively, for Inconel 718 doughs prepared using 5% aqueous solutions of PVA-1, PVA-2, and PVA-3. Despite the molecular weight differences of PVAs, the physical appearance and form of the doughs were similar when 5% aqueous solutions of PVAs were used as binders separately. The purpose is to get a dough-like consistency with the lowest binder amount possible, and the selection of the binder is based on the concept of polymer bridging that affects the stability of the particles. When high molecular weight polymer molecules attach to multiple particles at the same time, it's called bridging flocculation (Hogg, 2013). The suspensions can be dispersed further due to polymer bridging if the polymer concentration is relatively low (S. Kim et al., 2015). Thus, the solution of the highest molecular weight PVA, which is PVA-3, has been chosen as the binder solution in the formulation because the high molecular weight polymers have long chains that can provide bridges between more powder particles. This is also reflected in the PVA weight percentage given with respect to the metal powder for Inconel 718 dough prepared using the PVA-3 solution, which has the smallest value (0.13%) among the others. Thus, sufficient binding can be achieved with low binder amounts when polymers with high molecular weights are utilized. The long polymer chains can attach by forming physical bonds with the metal powder particles simultaneously (Hogg, 2013). This helps

maintain the structural integrity of the green bodies after surface texturing or molding. Figure 3.1 shows the image matrix of Inconel 718 doughs when 5% aqueous PVA-3 is used as a binder. The 3x3 image matrix shows visually how the dough structure changes with respect to solid loading and binder percentage. In the row of the image matrix, the binder percentage with respect to Inconel 718 powder started at its optimal dough formulation value and was intended to increase by 5%. For the first row and the third column element of the matrix, a 5% increase in binder percentage is unattainable, as even the water content in the binder solution exceeds what is necessary to satisfy both solid loading and binder constraints. Thus, the scanned range for the PVA-3 percentage concerning Inconel 718 powder in the image matrix is as follows: 0.13%, 0.18%, and 0.21%. The column of the matrix indicates the percentage of solid loading. The center of the column begins with the optimal solid loading percentage of 94.5%. Since the solid loading is notably high, the uppermost limit in the matrix is near this optimal value at 95.4%, while the minimum solid loading value recorded in the matrix is 93.0%.

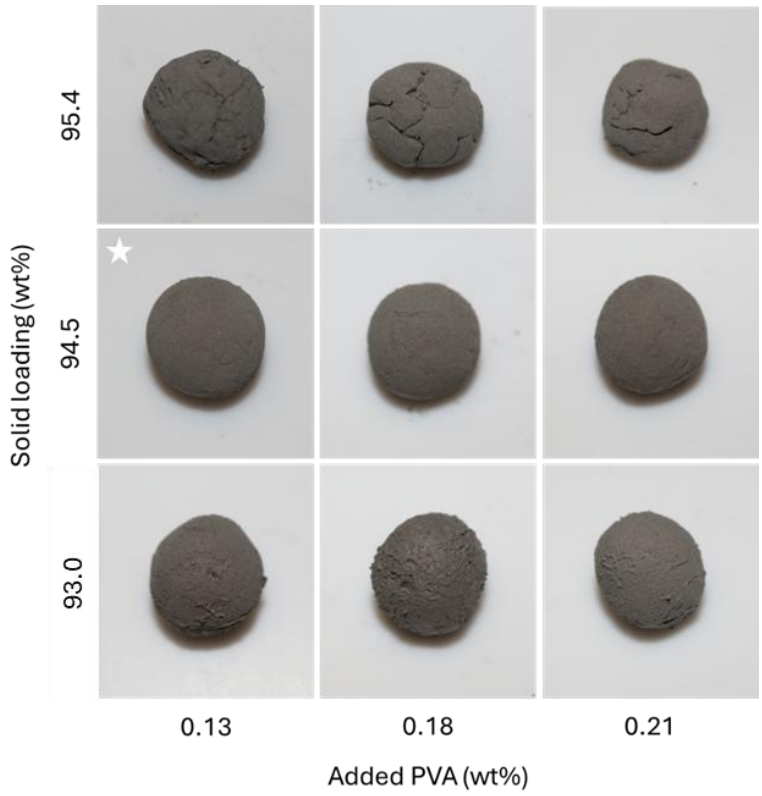

Figure 3.1. The image matrix of Inconel 718 doughs when 5% aqueous PVA-3 is used as a binder. The optimum formulation was indicated with a star.

As the solid loading increases, the amount of binder solution becomes insufficient, resulting in a significant deviation from a dough-like consistency and leading to large cracks. When the solid loading is kept constant at 94.5% by increasing the PVA, no significant physical change is observed. The dough with a solid loading of 94.5% and 0.13% binder has been selected as the optimal formulation because this formulation achieves the intended goal. When the solid loading is set to 93.0%, the dough-like consistency changes to a state that is between dough and paste, becoming wet and sticky.

3.2. Particle Size Analysis (PSA)

Particle size analysis (PSA) was performed to measure the floc size and observe the size distribution with and without the binder. For this purpose, the experiment was conducted on both the neat Inconel 718 powder and the powder with a 0.13% (wt% relative to metal powder) PVA addition, which represents the percentage in the optimum dough formulation. The particle size distributions are plotted in Figure 3.2.

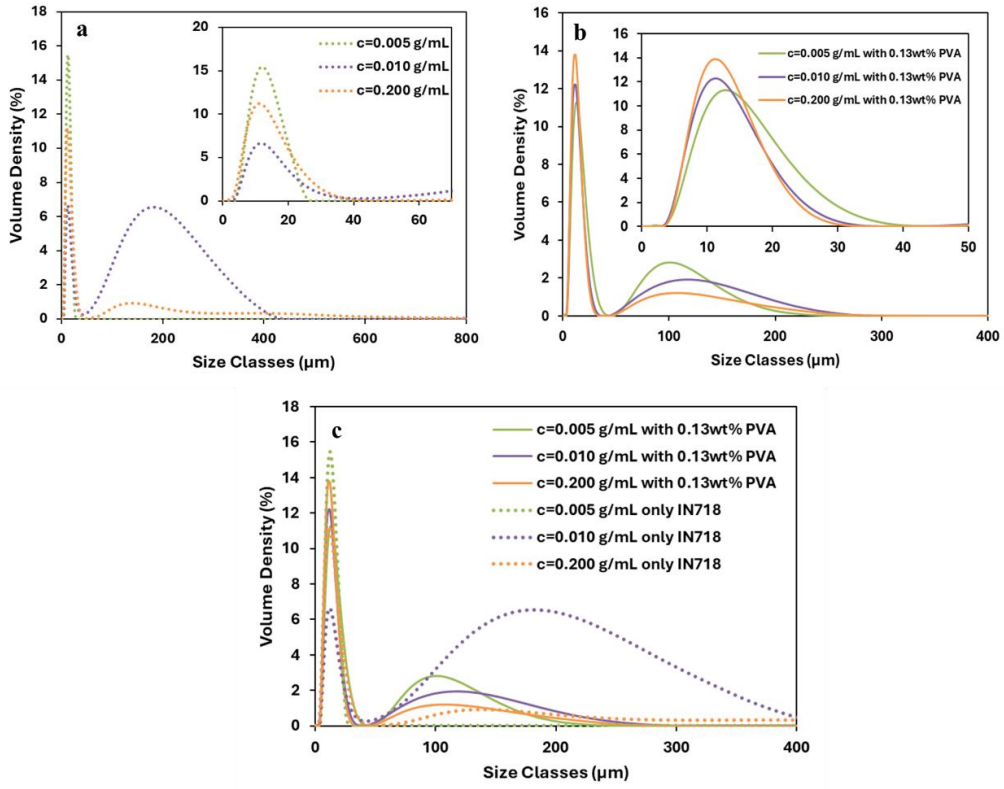

Figure 3.2. (a) The neat Inconel 718 powder, (b) Inconel 718 powder with 0.13 wt% PVA-3, and (c) Combination of plots a and b

The three concentrations of the solutions were prepared as 0.005 g (Inconel 718)/mL (DI water), 0.010 g/mL, which is twice the initial concentration, and 0.200 g/mL. In this way, the effect of concentration on floc size and the size distribution can be seen. The most diluted solution of Inconel 718 in the absence of PVA shows a unimodal distribution with the average floc size of approximately 11.6 μm. Dv indicates the percentage of the particles that have size values less than the stated value in the parentheses. When the concentration is twice, the size distribution becomes multimodal with Dv(10), Dv(50), and Dv(90) values of 7.84 μm, 27.3 μm, and 239 μm, respectively. While the first peak of 0.010 g/mL solution of Inconel 718 in the absence of PVA overlaps with its most dilute solution, the second peak indicates flocculation of the metal particles in the water. This flocculation may be a result of the uneven spreading of the powder during solution preparation. Once the metal particles adhered coherently to each other during the solution preparation, they could not be dispersed, despite the high-speed stirrer, and water could not diffuse among them. In the case of the most concentrated Inconel 718 solution without PVA, a multimodal distribution is again observed, with Dv(10), Dv(50), and Dv(90) values of 5.99 μm, 11.7 μm, and 26.5 μm, respectively. Although there is a second peak at 135 μm in the plot of neat 0.200 g/mL Inconel 718 solution, Dv(90) value and Figure 3.2.a indicate that most of the particles are concentrated at 11 μm. When 0.13 wt% PVA is added relative to the metal powder to the same concentrations of the Inconel 718 solutions, the first peaks, whose volume densities are the highest in each concentration, overlap with the neat Inconel 718 solutions at around 12 μm. The second peak in each concentration of PVA-added solutions indicates the formation of clusters, with an average size of approximately 110 μm. Figure 3.3 compares each concentration of solution with and without the PVA. The effect of binder in the coagulation of metal powders is pronounced in the most diluted Inconel 718 solution. While the neat Inconel solution with 0.005 g/mL concentration has a unimodal distribution, after the addition of the binder, the polymer chain can cover the surface of some metal powder particles, resulting in larger-sized particles being observed. As the concentration of metal particles increases, the second peaks can shift to smaller sizes, indicating that the PVA can effectively disperse the metal particles.

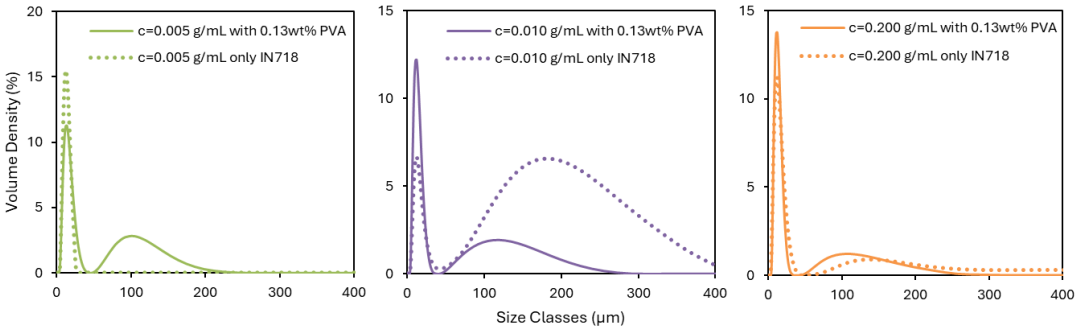

Figure 3.3. Each concentration of Inconel 718 solution with and without the PVA

3.3. The Rheology of Doughs

The physical appearance and form of the doughs are relatively similar despite the molecular weight differences of PVAs, as stated in Section 3.1. The rheological analysis was performed on Inconel 718 doughs prepared with each PVA solution, considering that this indistinguishability can be elucidated by revealing the effect of the molecular weight of the binder. Flow curve measurements were conducted first to determine the viscosity of Inconel 718 doughs prepared with 5% aqueous solutions of PVAs. The weight percentages for solid loading in Inconel 718 doughs prepared using 5% aqueous solutions of PVA-1, PVA-2, and PVA-3 are 94.8%, 94.2%, and 94.5%, while the PVA weight percentages relative to the metal powder are 0.15%, 0.15%, and 0.13%, respectively. Three measurements were conducted with different samples from the same batch of each dough, and the results were averaged for viscosity, whose plot with respect to shear rate is given in Figure 3.4. As the shear rate increases, the viscosity of the dough, independent of the binder used, decreases, exhibiting shear thinning (pseudoplastic) behavior. The polymer chains are aligned as the shear rate increases and the internal friction decreases. The viscosity plots almost overlap, and the effect of the molecular weight of the binder on the dough could not be observed. This can be attributed to the notably high solid loading (>90 wt%) and very low binder amount (~0.15 wt%). Hence, further analysis of the rheology continues with the Inconel 718 dough prepared using the highest molecular weight PVA, namely PVA-3, as discussed in Section 3.1.

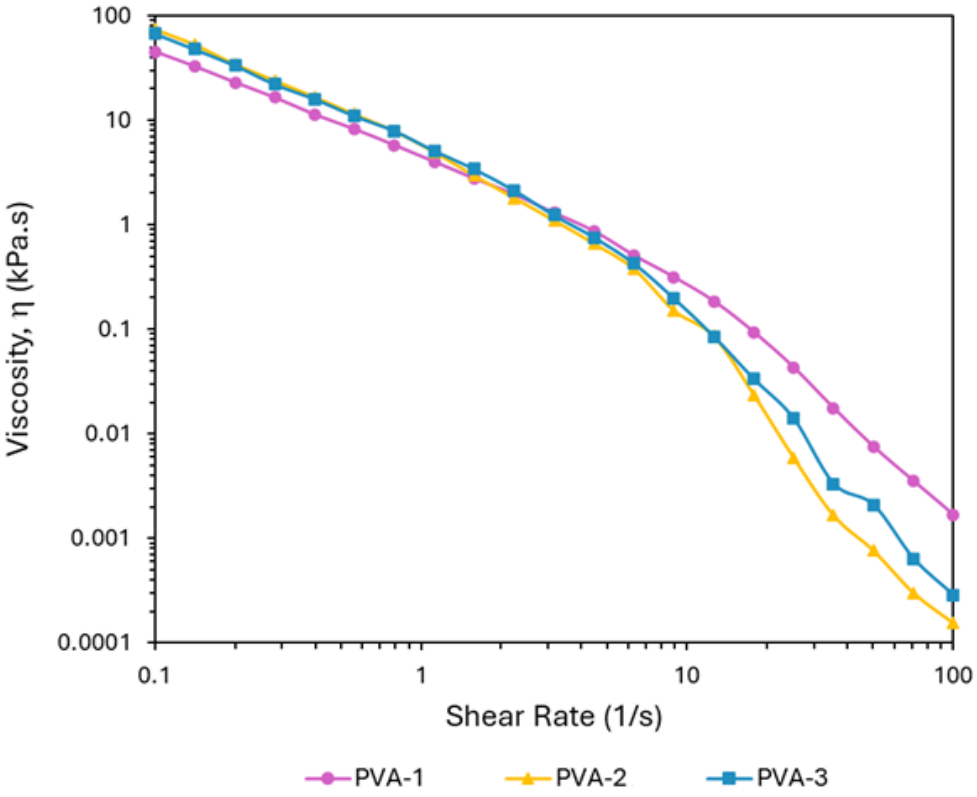

Figure 3.4. Flow curve measurements for each dough

The amplitude sweep analysis was conducted on Inconel 718 dough prepared by PVA-3 to determine the viscoelastic properties. To be more precise, the analysis was performed to determine the structural durability limit of the dough and the region at which the dough demonstrates linear viscoelastic behavior. The importance of the linear viscoelastic region (LVER) is that it defines the region where the structure of the material has not been deformed, and it is indicated by the constant loss and storage moduli despite the increasing strain. Thus, the rheological measurements, such as frequency sweep analysis, conducted in this region become reliable. The plot of the loss (G'') and storage (G') modulus with respect to the shear strain is given in Figure 3.5. The LVER is not observed in the plot. At low shear strains, namely less than 0.10%, the storage modulus is greater than the loss modulus. The storage modulus is referred to as the elastic component, while the loss modulus represents the viscous component. Hence, the dough in the region where the shear strain is smaller than 0.10% shows solid-like behavior. The loss and storage moduli intersect at a strain of 0.11%, corresponding to a yield point of 2.53 MPa. After the yield point, the loss modulus is greater than the storage modulus and the dough shows viscous flow behavior. The dough shows zig-zag behavior in the strain range of 0.1% to

1.0%. At approximately 0.1–1% strains, these doughs may undergo some inter-particle bond loosening or repacking. These phenomena create temporary, irregular fluctuations in G' and G", which show themselves as a zig-zag pattern in the plot.

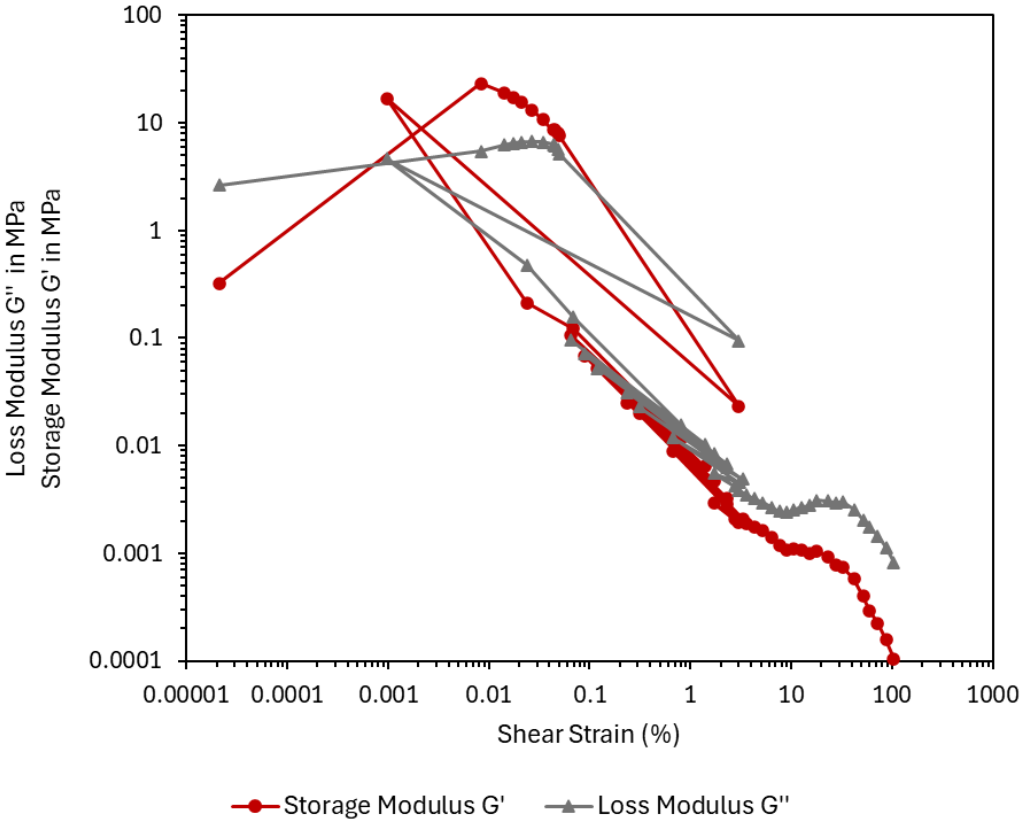

Figure 3.5. Amplitude sweep analysis on Inconel 718 dough prepared by PVA-3

3.4. Thermogravimetric Analysis (TGA)

TGA was performed to adjust the sintering profile and ensure the complete removal of the binder. In this regard, TGA was conducted on the crystalline form of PVA-3 as received from the supplier and Inconel 718 dough prepared with PVA-3. The results are given in Figure 3.6. The mass of the crystalline PVA-3 decreases by 2.59% at the end of 80°C, which accounts for the removal of physically bound water and other volatile substances. Most of the crystalline PVA-3, specifically 89.53%, degraded thermally within the temperature range of 80°C to 550°C. This result suggests that the complete removal of the binder during the sintering occurs at temperatures around 600°C. The Inconel 718 dough with PVA-3, on the other hand, loses 3.88% of its mass at 110°C. Since

the solid loading of the dough is considerably high (94.5%), the step for the mass loss of PVA inside the dough cannot be observed.

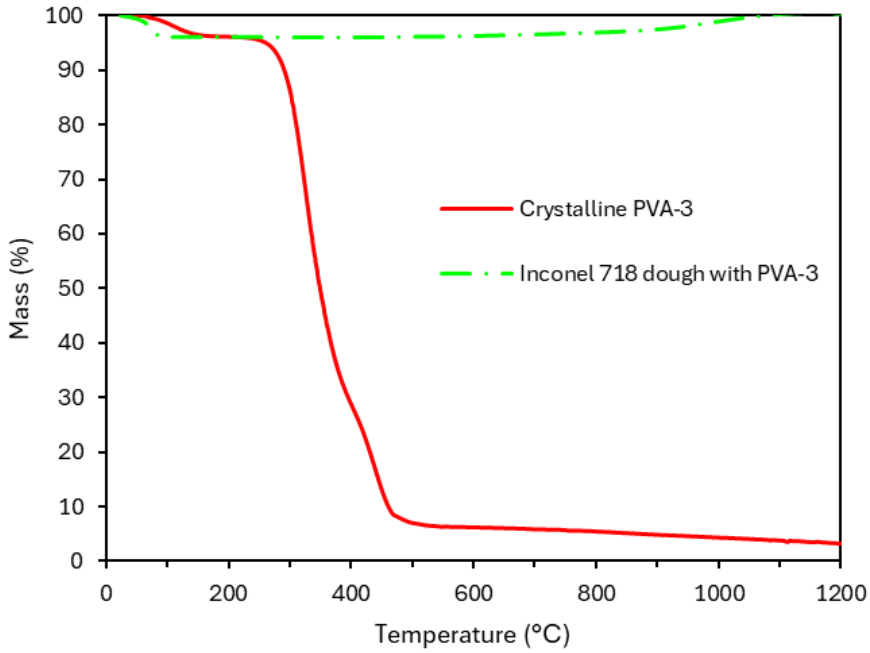

Figure 3.6. TGA results

3.5. Surface Structuring and SEM/EDS

The Inconel 718 dough with PVA-3 binder is prepared and spread onto the laboratory bench using a rolling pin for surface structuring with 3D printed snowflake and pyramidal stamps, wheels with patterns on them, and a roller, which are given in Figure 2.1. The application of the 3D printed snowflake stamp and wheel onto the dough, as well as its form after sintering, can be seen in Figure 3.7. They are sintered with the sintering profile given in Figure 2.3.a without the use of a flowmeter due to unavailability, and the Argon flow was adjusted solely by setting the regulator pressure to a minimum value of less than 0.1 bar. Hence, the flow cannot be controlled during this sintering; the concavity of the structured surface for the sintered body can be seen in Figure 3.7.b, especially for the wheel applied sintered body. Heat is transferred to the bottom of the sample via conduction, and the heat on the top of the sample is dissipated by the Argon gas flow via convection. Thus, the concave shape of the sample at the end of the sintering was attributed to this temperature difference, resulting from the high flow rate that could not

be controlled. Following this experiment, the flowmeter was supplied for use in further sintering processes.

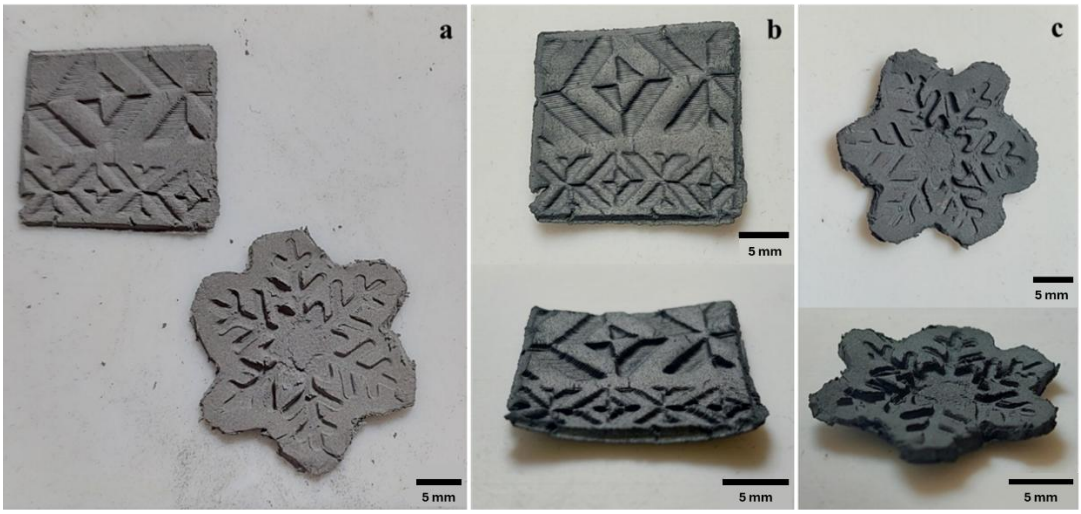

Figure 3.7. Snowflake stamp and wheel applications (a) Green body, (b-c) Sintered bodies from different views

For the roller, it has taken advantage of the inherent layer-by-layer deposition property of the 3D printer, which leaves unwanted textures on the print depending on the resolution of the printer. These unwanted textures of the roller can be utilized to create a sharkskin-like texture, as given in Figure 3.8. The interval between each line is 200 micrometers in size, which is precisely the same as the interval between the layers of the 3D printed roller. The Inconel 718 dough prepared with PVA-3 preserves the surface structuring applied to it, thereby showing high fidelity in both its green and sintered bodies. The same sintering profile (Figure 2.3.a) was used but with 200 cc/min Argon flow rate.

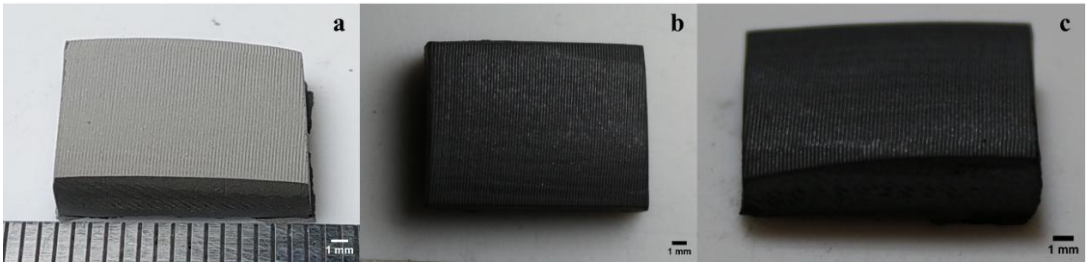

Figure 3.8. (a) Sharkskin-like texture on green body, (b-c) Views from the sintered body

The SEM images of the green body, whose surface is structured by the roller as sharkskin-like texture, are given in Figure 3.9. The spacing between the lines is equal, and the

transformation of the strips onto the dough is successfully achieved by rolling the 3D printed roller on the green body. This process demonstrates that Inconel 718, one of the most difficult-to-machine metals, can be structured effortlessly by hand in just a short time (~2 minutes) at room temperature and atmospheric pressure, without the need for specialized equipment. As the magnification increased, the spherical form of the Inconel 718 powders could be seen. The particles are sticking together, showing their size and shape distribution, as well as the pores between them. The SEM images of the sintered body given in Figure 3.10 shows that the surface texture has been preserved after sintering, and spherical powder particles form grains by densification.

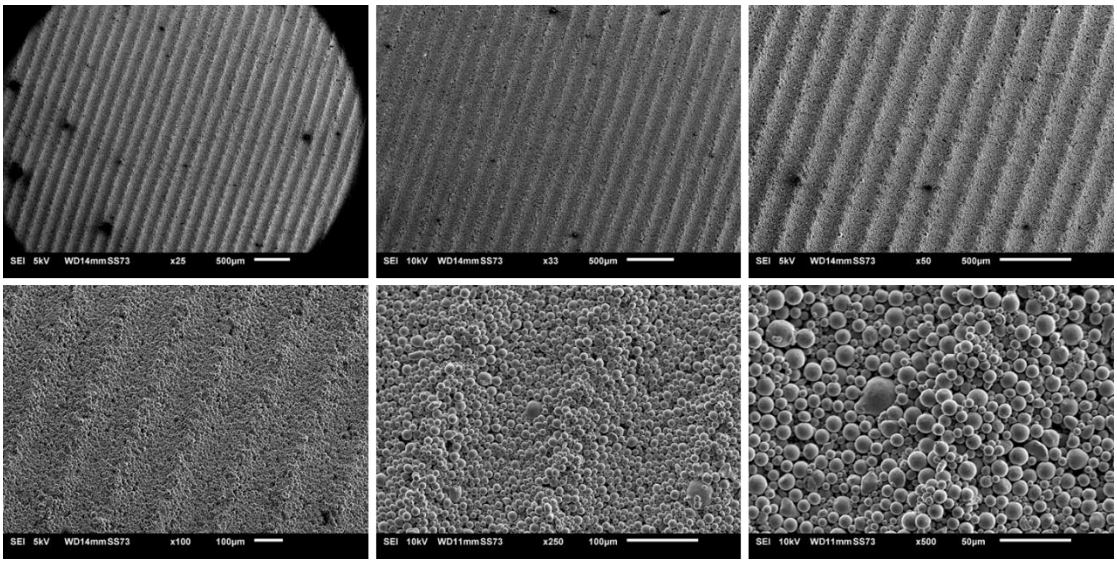

Figure 3.9. SEM images of the green body, whose surface is structured by the roller as sharkskin-like texture

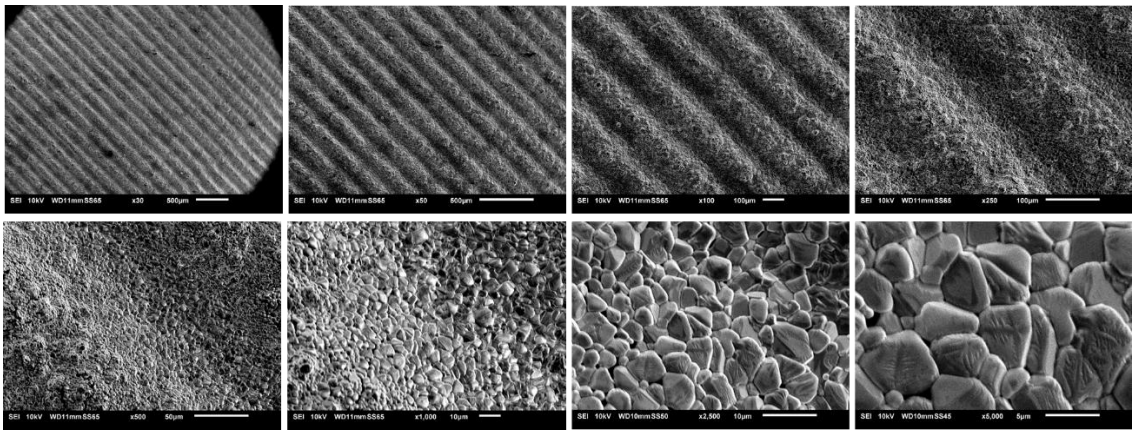

Figure 3.10. SEM images of the sintered body, whose surface is structured by the roller as sharkskin-like texture

EDS analysis was performed on the green and sintered bodies of the sharkskin-like textured Inconel 718. The result is given in Figure 3.11. The sharp oxygen peak evolves after sintering, while the small peaks for Nb, Al, Ti, and S disappear. This can also be seen in Table 3.1 in which the elemental compositions obtained from EDS analysis are given in weight percentages for green and sintered bodies. The chemical and physical properties of these elements can explain the reason for the unidentified elements that occur after sintering. Sulfur (S) is a volatile element with a very low boiling point, namely 445°C (*Sulfur | S | CID 5362487 - PubChem*, n.d.), and it is expected that it leaves the structure at high temperatures, 1150°C, during the sintering. Thus, sulfur cannot be detected by EDS after sintering. Aluminum (Al), on the other hand, has a relatively high boiling point, 2327℃ (*Aluminum | Al | CID 5359268 - PubChem*, n.d.). It has a high affinity towards oxygen, which is available in the structure as water. Al particles can react and form Al_2O_3. However, the initially detected Al in the structure is already low (0.48 wt%), and it has a low atomic number compared to other metals in the structure, which can diffuse to the interstitial regions. Considering these factors, EDS could not identify Al after sintering due to its low concentration, diffusion into inner areas, and suppression of its signal in the presence of heavy metals, such as Ni and Cr. Hence, it could not be detected even though it is present in the structure. Niobium (Ni) and titanium (Ti) have a tendency to form stable secondary phases. At high temperatures, they can react with oxygen or carbon to form oxide or carbide precipitates, which can be distributed within the grains or at the grain boundaries in the structure. Thus, Nb and Ti could not be detected by EDS after sintering because their concentration in the structure is already low, and they can be drawn to the inner regions via atomic diffusion. Moreover, limitations of EDS should be taken into consideration.

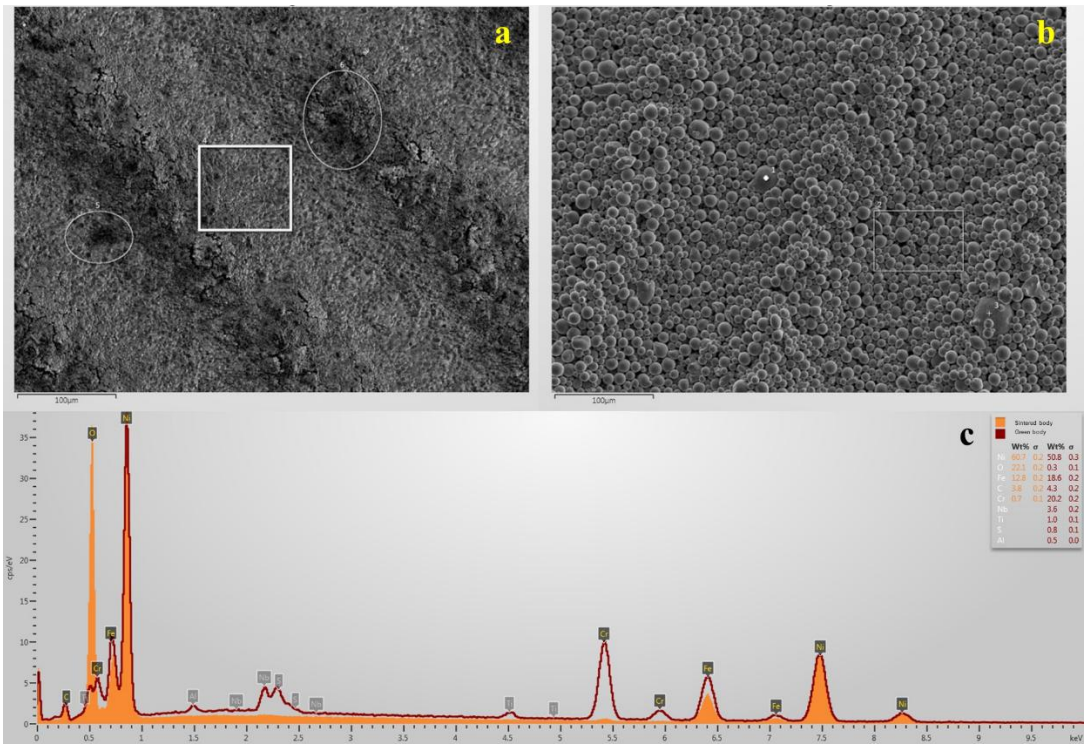

Figure 3.11. (a) Sharkskin-like textured sintered body. The region scanned for EDS is highlighted by the white rectangle. (b) Sharkskin-like textured green body. The white point indicates the scanned region for EDS. (c) EDS plots. The orange highlighted plot belongs to the sintered body, while the red plot belongs to the green body.

Table 3.1. The EDS elemental composition (in weight percentages) of sharkskin-like textured Inconel 718 for its green and sintered bodies

	Green Body	**Sintered**
	wt%	**wt%**
Ni	50.75	60.7
O	0.27	22.06
Fe	18.59	12.77
C	4.33	3.77
Cr	20.2	0.71
Nb	3.63	
Ti	1.01	
S	0.75	
Al	0.48	
TOTAL	**100.0**	**100.0**

Another surface structuring of Inconel 718 dough was conducted by the pyramidal stamp as given in Figure 3.12. The layers of 3D printed pyramidal stamp can be seen on the green body, and they are preserved during sintering. The simultaneous formation of side

structures, namely layers, in addition to the main structure, pyramids, further increases the surface area and can be utilized in fields that require extended surfaces, such as the plates for heat exchangers.

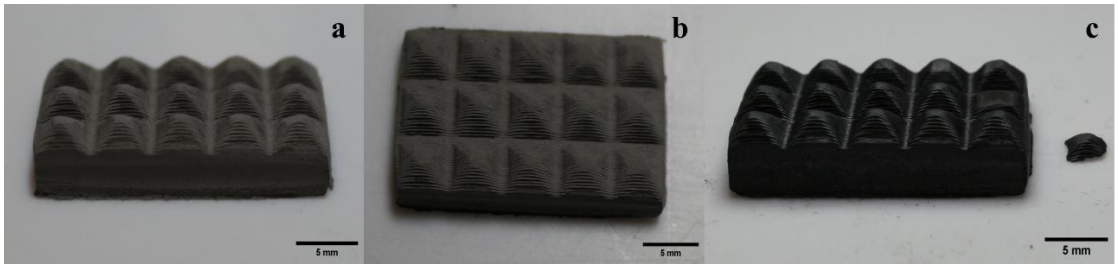

Figure 3.12. (a-b) Green body (c) Sintered body

The only defect observed after sintering is that one of the pyramidal edges was ruptured, which can also be seen in Figure 3.12.c. The SEM images for that region are given in Figure 3.13. This sample was sintered with the sintering profile given in Figure 2.3.a with 200 cc/min Argon flow rate. As the magnification is increased, the spherical particles become visible, indicating that the sintering is incomplete. On the other hand, the SEM images from a different region of the pyramids, as given in Figure 3.14, present the grains formed on the surface at x1000 magnification. Hence, it can be stated that the inner sides cannot be sintered as effectively as the outer surface.

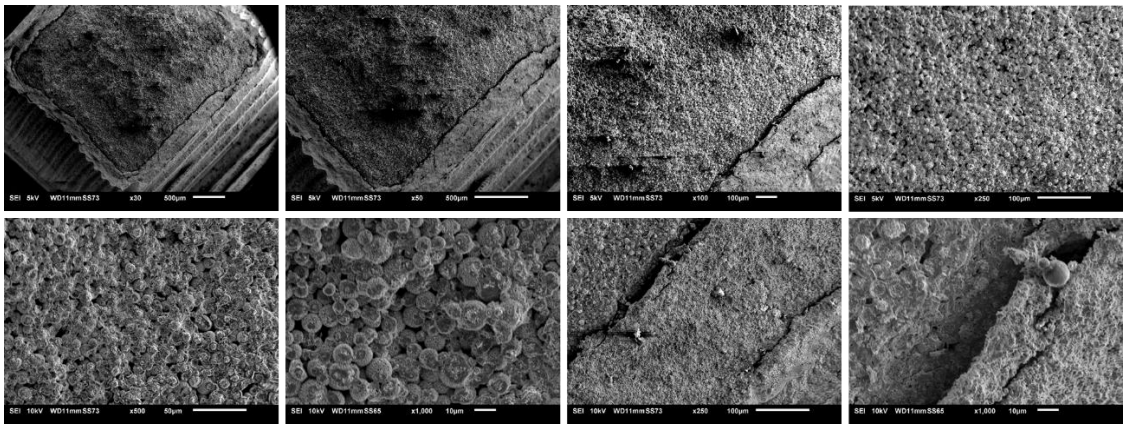

Figure 3.13. SEM images of the ruptured pyramid

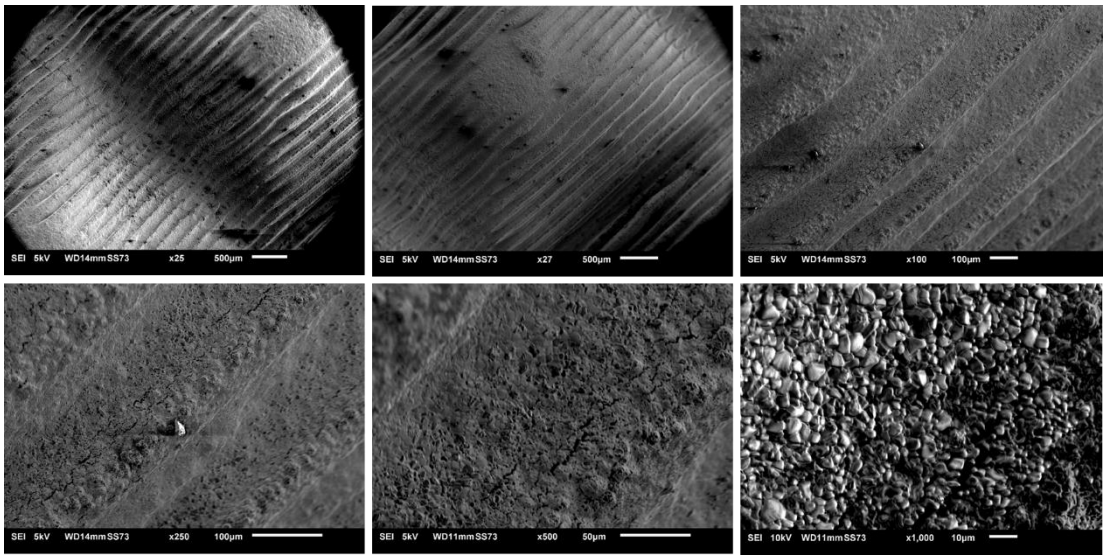

Figure 3.14. SEM images of the pyramids from another region

3.6. Density and Volume of Green and Sintered Bodies

The five samples of Inconel 718 dough with PVA-3 binder were prepared. The formulation of dough is the starred composition in Figure 3.1. The sintering profile given in Figure 2.3.a with 200 cc/min Argon flow rate was applied. The volumes of the doughs and their sintered bodies were measured using the gas pycnometer, as explained in Section 2.5.3. The samples and the summary of the results are presented in Figure 3.15 while the sample-wise representation of the properties is given in Figure 3.16. The volume expansion and mass increase can be attributed to oxidation, as indicated by the EDS results (Figure 3.11.c and Table 3.1). Since the mass increase (5.5%) cannot overcome the volume increase (9.1%), a 3.3% decrease in density is observed.

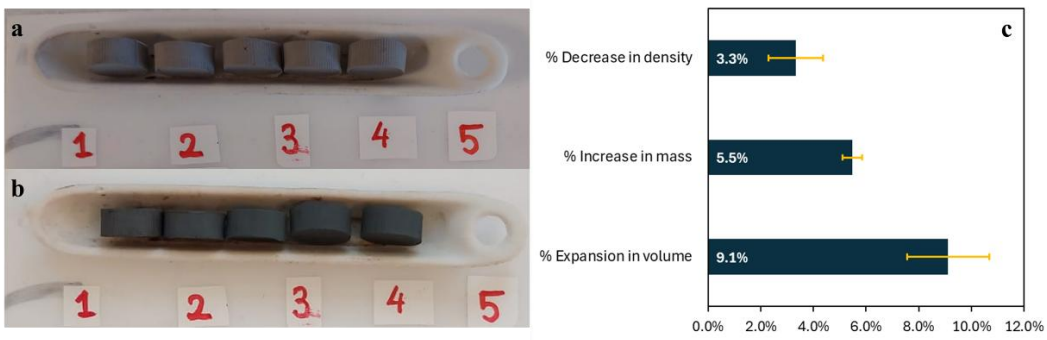

Figure 3.15. (a) Green body (b) Sintered body (c) Summary of the property changes after sintering

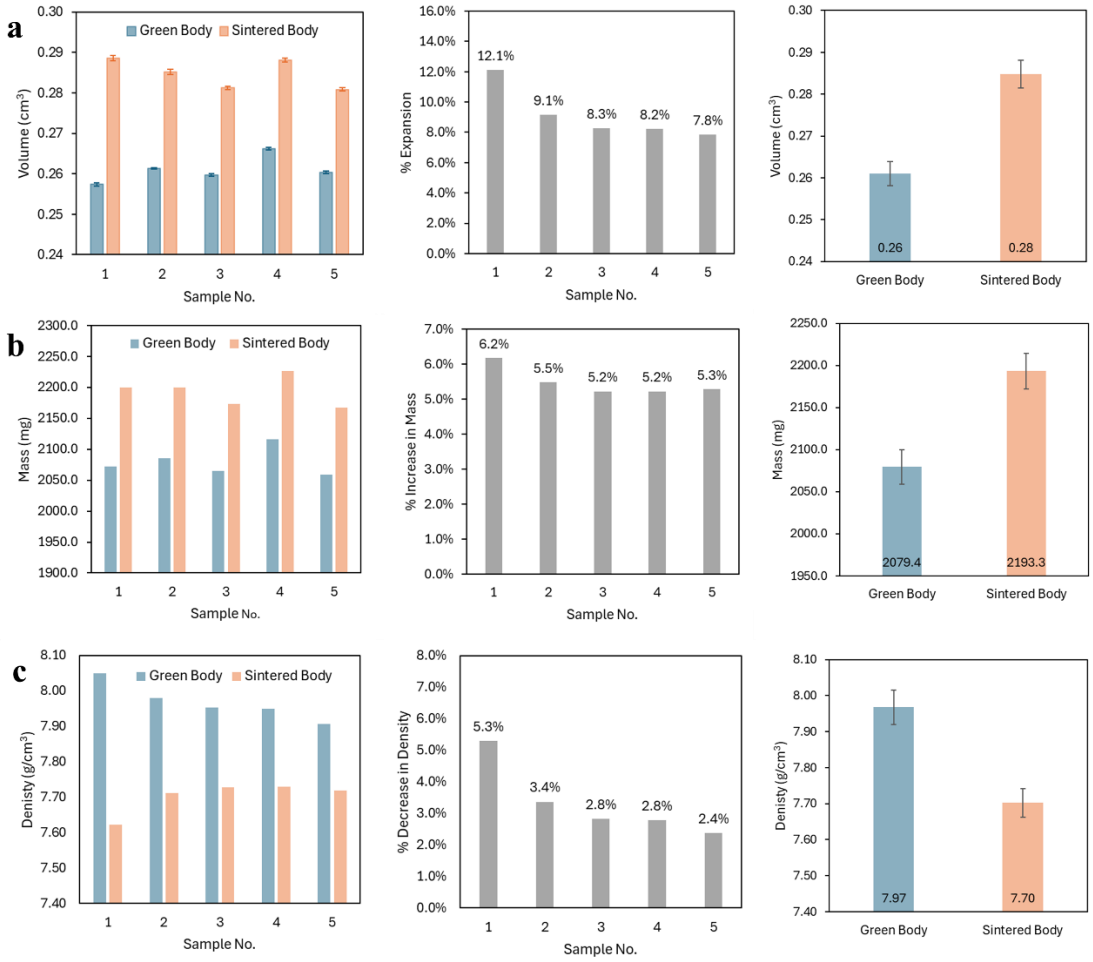

Figure 3.16. Sample-wise property changes and their averages: (a) volume, (b) mass, (c) density

3.7. XRD Analysis

The XRD analysis was conducted on the Inconel 718 powder, green body, and the sintered body of Inconel 718 prepared by PVA-3. The XRD pattern of the sintered body belongs to the surface structured Inconel 718, which is given in Figure 3.7.a. The XRD plots are provided in Figure 3.17. The PDF cards for all the substances are provided in Appendix A. The Inconel powder and the green body have the same XRD pattern, namely $FeCr_{0.29}Ni_{0.16}C_{0.06}$, $Fe_{0.64}Ni_{0.36}$, and Fe_3Ni_2. While Nb, Ti, Al, and S are detected by EDS even at low quantities in the green body, the peaks for these metals cannot be encountered in XRD analysis. Moreover, peaks corresponding to Mn, Zn, and Ti metals are observed

in the XRD results after sintering. Mn and Zn metals can be attributed to the sample holder. The sintered Inconel 718 couldn't cover the whole region on the holder, and the signals from the metallic holder might also reach the detector.

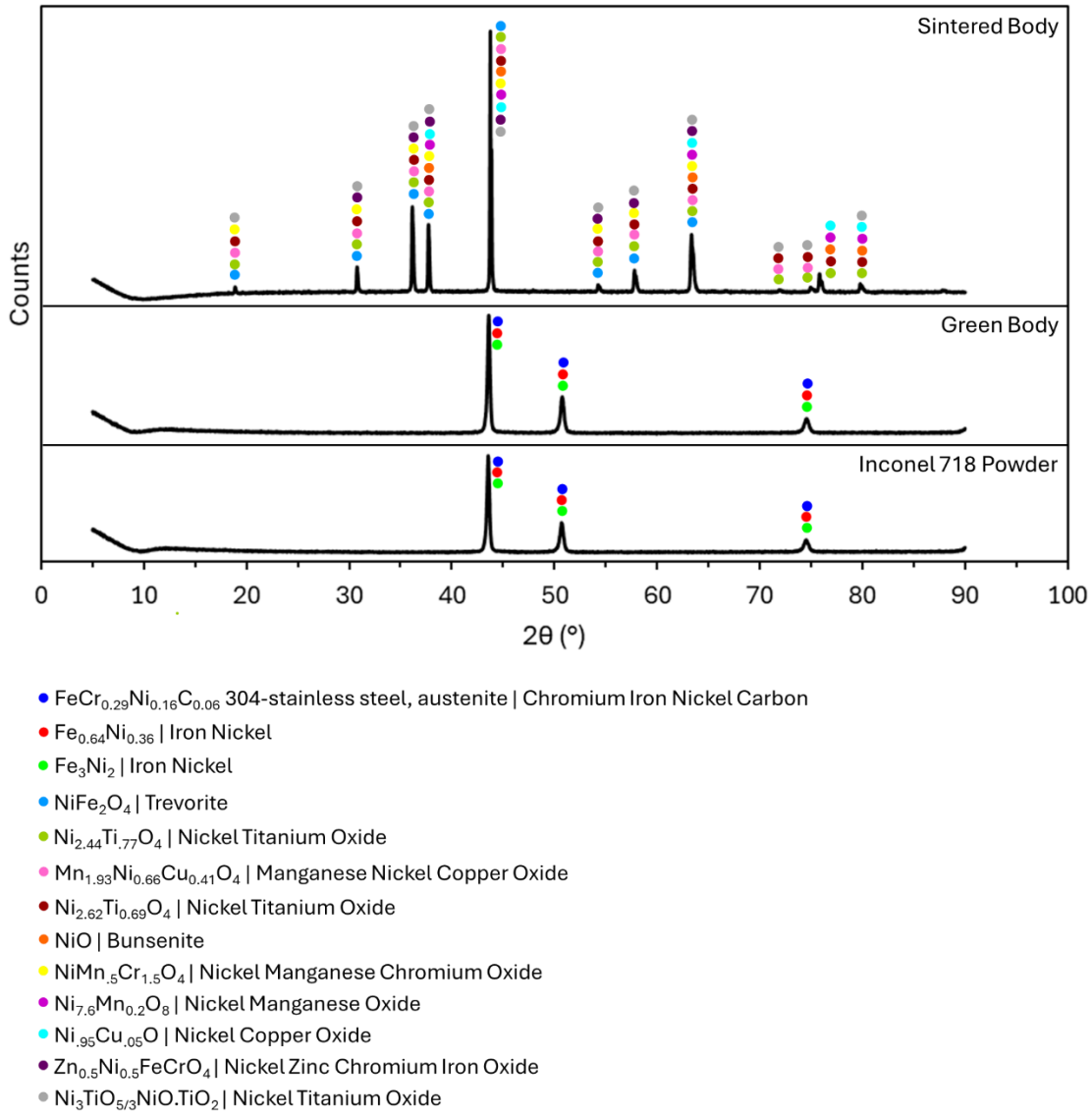

Figure 3.17. XRD results

3.8. Sintering and Mechanical Properties

Mechanical properties were tested by using the three-point bending configuration. The sintering profile has a profound effect on the mechanical properties. The results are

presented in T. The bending stress is calculated using Equation 1, where the span length for the support is maintained at 39.00 mm.

$$\sigma = \frac{3 \times F_{max} \times L}{2 \times b \times d^2} \quad (1)$$

Table 3.2. Mechanical properties according to the sintering profiles

Sintering Profile	Sample No.	F_{max} (N)	σ (MPa)
Figure 2.3.a	1	44.12	11.43
	2	17.19	4.55
	3	13.50	3.62
	4	121.26	33.67
	Average	49.02 ± 43.35	13.32 ± 12.13
Figure 2.3.b	The test couldn't be performed due to the crumbly form of the specimens.		
Figure 2.3.c	The samples could be broken by hand.		
Figure 2.3.d	1	343.42	95.00
	2	263.17	70.21
	Average	303.30 ± 40.13	82.60 ± 12.40
Figure 2.3.e	1	230.27	56.83
	2	198.06	48.90
	Average	214 ± 16.11	52.87 ± 3.97

These bending stress values are too low for sintered Inconel 718 samples, which are reported as 1807 ± 52 MPa (Hidalgo et al., 2024). The highest achievable bending stress is 95.00 MPa when evaluated on a sample-by-sample basis. The possible reasons and observations can be listed as follows:

- Even though the sintering was conducted under an Argon flow to avoid oxidation of metal species in the structure, the water inside the formulation joined the structure. It negatively affected the bending strength of the material.

- After preparation of the dough, the mold was filled by hand, which might have led to pores inside the green body that could not be confined during the sintering process and thereby reduced the bending stress.
- The presence of surface cracks and roughness might lead to low mechanical properties, so polishing should be performed before the test.
- 1150°C was insufficient for the atomic diffusion, regardless of the duration at this temperature. This is also indicated by the subsequent trial at 1260°C, which leads to higher bending stress values.

CHAPTER 4

4. CONCLUSIONS

Near-net shaping of advanced materials, such as Inconel 718, is currently conducted using energy-intensive methods that require specialized and costly equipment. Moreover, the most advanced additive manufacturing methods can process only one workpiece at a time, resulting in extended work times that are not suitable for large-scale production. This study proposes a method for forming a green body by utilizing the formation of malleable dough from Inconel 718 powder and polyvinyl alcohol (PVA) dissolved in water. It reduces the complexity in processing in such a way that it enables giving shapes to the green body by hand or mold, and onto the metal surface by stamps, wheels, or rollers with patterns on them, which is similar to shaping clay. For this purpose, Inconel 718 dough was prepared with a solid loading of 94.5% using the highest molecular weight PVA, which has a molecular weight of 85,000–146,000 g/mol, as a binder at 0.13 wt% with respect to the powder. PSA showed that the PVA covers the surface of the metal powders effectively in the most diluted Inconel 718 solution, with the emergence of large sizes after the addition of the PVA solution. The effect of the molecular weight of PVAs cannot be observed in the viscosity determination of the doughs, as they all behaved as shear-thinning fluids with nearly the same path in the viscosity plot. The temperature for the binder removal in the sintering profiles is ensured by TGA analysis. Surface structuring demonstrates that the inherent layer-by-layer deposition property of the 3D printer can be utilized to create a sharkskin-like texture with 200 μm spacing. The pattern created on the surface is transformed with high fidelity and preserved after sintering. There has been a 9.1% volume expansion and a 5.5% increase in mass after sintering, attributed to oxidation, which leads to a 3.3% decrease in density. XRD analysis revealed the oxides formed in the structure after sintering. Although many sintering profiles have been tried

to achieve better mechanical properties, the highest bending stress obtained was 95 MPa at a force of 343.42 N. This outcome does not meet the expected standards, and modifications to the sintering profile are necessary to align the reported values and even potentially exceed them. Despite the low mechanical properties obtained, this process demonstrates that Inconel 718, one of the most difficult-to-machine metals, can be structured effortlessly by hand in just a short time (~2 minutes) at room temperature and atmospheric pressure, without the need for specialized equipment. The study establishes a foundation for this method. It paves the way for further advancements in the process, making it accessible even in a frugal environment for individuals without domain knowledge.

BIBLIOGRAPHY

Aluminum | Al | CID 5359268 - PubChem. (n.d.). Retrieved 11 June 2025, from https://pubchem.ncbi.nlm.nih.gov/compound/5359268#section=Boiling-Point

Antona, P. L., & Mapelli, C. (2001). Hot Isostatic Pressing (HIP): the State of the Art & Improvement on Two Steels. *Metallurgical Science and Tecnology*, *19*(2). https://www.fracturae.com/index.php/MST/article/view/1076

Arzt, E., Quan, H., McMeeking, R. M., & Hensel, R. (2021). Functional surface microstructures inspired by nature – From adhesion and wetting principles to sustainable new devices. *Progress in Materials Science*, *120*, 100823. https://doi.org/10.1016/J.PMATSCI.2021.100823

Atkinson, H. V., & Davies, S. (2000). Fundamental aspects of hot isostatic pressing: An overview. *Metallurgical and Materials Transactions A: Physical Metallurgy and Materials Science*, *31*(12), 2981–3000. https://doi.org/10.1007/S11661-000-0078-2/METRICS

Bixler, G. D., & Bhushan, B. (2012). Bioinspired rice leaf and butterfly wing surface structures combining shark skin and lotus effects. *Soft Matter*, *8*(44), 11271–11284. https://doi.org/10.1039/C2SM26655E

Bixler, G. D., & Bhushan, B. (2013). Fluid drag reduction with shark-skin riblet inspired microstructured surfaces. *Advanced Functional Materials*, *23*(36), 4507–4528. https://doi.org/10.1002/adfm.201203683

Bocanegra-Bernal, M. H. (2004). Hot isostatic pressing (HIP) technology and its applications to metals and ceramics. *Journal of Materials Science*, *39*(21), 6399–6420. https://doi.org/10.1023/B:JMSC.0000044878.11441.90/METRICS

Campbell, J. (2023). A Future for Vacuum Arc Remelting and Electroslag Remelting—A Critical Perspective. *Metals 2023, Vol. 13, Page 1634*, *13*(10), 1634. https://doi.org/10.3390/MET13101634

Choudhury, A. (1992). State of the Art of Superalloy Production for Aerospace and Other Application Using VIM/VAR or VIM/ESR. *Isij International*, *32*(5), 563–574. https://doi.org/10.2355/ISIJINTERNATIONAL.32.563

Dini, F., Ghaffari, S. A., Jafar, J., Hamidreza, R., & Marjan, S. (2020). A review of binder jet process parameters; powder, binder, printing and sintering condition. *Metal Powder Report*, *75*(2), 95–100.

https://doi.org/10.1016/J.MPRP.2019.05.001;REQUESTEDJOURNAL:JOURNAL:MPRP;ISSUE:ISSUE:10.1016/S0026-0657(20)X0003-8;WGROUP:STRING:PUBLICATION

Geiger, M., Kleiner, M., Eckstein, R., Tiesler, N., & Engel, U. (2001). Microforming. *CIRP Annals*, *50*(2), 445–462. https://doi.org/10.1016/S0007-8506(07)62991-6

Ghimire, A., Dahl, R. B., Shen, S. F., & Chen, P. Y. (2024). Shark Skin Denticles: From Morphological Diversity to Multi-functional Adaptations and Applications. *Advanced Functional Materials*, *34*(35), 2307121. https://doi.org/10.1002/adfm.202307121

Gibson, I., Rosen, D., Stucker, B., & Khorasani, M. (2021). Binder Jetting. *Additive Manufacturing Technologies*, 237–252. https://doi.org/10.1007/978-3-030-56127-7_8

Gokuldoss, P. K., Kolla, S., & Eckert, J. (2017). Additive Manufacturing Processes: Selective Laser Melting, Electron Beam Melting and Binder Jetting—Selection Guidelines. *Materials 2017, Vol. 10, Page 672*, *10*(6), 672. https://doi.org/10.3390/MA10060672

Hahn, L., Meyer, P., Bade, K., Hein, H., Schulz, J., Löchel, B., Scheunemann, H. U., Schondelmaier, D., & Singleton, L. (2005). MODULIGA: The LIGA process as a modular production method-current standardization status in Germany. *Microsystem Technologies*, *11*(4–5), 240–245. https://doi.org/10.1007/S00542-004-0368-5/METRICS

Herrmann, M., & Räthel, J. (2021). Hot Pressing and Hot Isostatic Pressing. *Encyclopedia of Materials: Technical Ceramics and Glasses: Volume 1-3*, *1*, 270–277. https://doi.org/10.1016/B978-0-12-818542-1.00039-4

Hidalgo, J., González-Velázquez, V., Naranjo, J. A., Berges, C., Vázquez, E., & Herranz (Ca), G. (2024). Towards mass production of graphene-reinforced inconel 718 by powder injection moulding. *Results in Engineering*, *22*, 102233. https://doi.org/10.1016/J.RINENG.2024.102233

Ho, K. H., & Newman, S. T. (2003). State of the art electrical discharge machining (EDM). *International Journal of Machine Tools and Manufacture*, *43*(13), 1287–1300. https://doi.org/10.1016/S0890-6955(03)00162-7

Hogan, L. M. (2001). Crystals, Dendritic Solidification of. *Encyclopedia of Materials: Science and Technology*, 1913–1918. https://doi.org/10.1016/B0-08-043152-6/00348-X

Hogg, R. (2013). Bridging Flocculation by Polymers. *KONA Powder and Particle Journal*, *30*, 3–14. https://doi.org/10.14356/KONA.2013005

Hormes, J., Göttert, J., Lian, K., Desta, Y., & Jian, L. (2003). Materials for LiGA and LiGA-based microsystems. *Nuclear Instruments and Methods in Physics Research Section B: Beam Interactions with Materials and Atoms*, *199*, 332–341. https://doi.org/10.1016/S0168-583X(02)01571-9

Hruby, J. (2001). Liga technologies and applications. *MRS Bulletin*, *26*(4), 337–340. https://doi.org/10.1557/MRS2001.76/METRICS

Ikumapayi, O. M., Akinlabi, E. T., Onu, P., & Abolusoro, O. P. (2020). Rolling operation in metal forming: Process and principles – A brief study. *Materials Today: Proceedings*, *26*, 1644–1649. https://doi.org/10.1016/J.MATPR.2020.02.343

Ito, T., & Okazaki, S. (2000). Pushing the limits of lithography. *Nature*, *406*(6799), 1027–1031. https://doi.org/10.1038/35023233;KWRD=SCIENCE

John, M. M., & Hanief, M. (2023). Frictional noise mitigation using synergetic approach of laser surface texturing and bio-lubrication. *Tribology International*, *178*, 108056. https://doi.org/10.1016/J.TRIBOINT.2022.108056

Khaskhoussi, A., Calabrese, L., Patané, S., & Proverbio, E. (2021). Effect of Chemical Surface Texturing on the Superhydrophobic Behavior of Micro–Nano-Roughened AA6082 Surfaces. *Materials 2021, Vol. 14, Page 7161*, *14*(23), 7161. https://doi.org/10.3390/MA14237161

Khodabandeh, A. R., Jahazi, M., Yue, S., & Bocher, P. (2005). Impact Toughness and Tensile Properties Improvement through Microstructure Control in Hot Forged Nb-V Microalloyed Steel. *ISIJ International*, *45*(2), 272–280. https://doi.org/10.2355/ISIJINTERNATIONAL.45.272

Kim, J. H., Chang, S. S., & Lim, G. (2014). A simple approach for an ultra-precise patterning using deep x-ray lithography with a micron-patterned x-ray mask. *International Journal of Precision Engineering and Manufacturing*, *15*(11), 2385–2390. https://doi.org/10.1007/S12541-014-0604-6/METRICS

Kim, S., Hyun, K., Moon, J. Y., Clasen, C., & Ahn, K. H. (2015). Depletion stabilization in nanoparticle-polymer suspensions: Multi-length-scale analysis of microstructure. *Langmuir*, *31*(6), 1892–1900. https://doi.org/10.1021/LA504578X/ASSET/IMAGES/LA-2014-04578X_M008.GIF

Koch, K., Bhushan, B., & Barthlott, W. (2009). Multifunctional surface structures of plants: An inspiration for biomimetics. *Progress in Materials Science*, *54*(2), 137–178. https://doi.org/10.1016/j.pmatsci.2008.07.003

Leitz, K. H., Singer, P., Plankensteiner, A., Tabernig, B., Kestler, H., & Sigl, L. S. (2017). Multi-physical simulation of selective laser melting. *Metal Powder Report*, *72*(5), 331–338. https://doi.org/10.1016/J.MPRP.2016.04.004

Leśniak, D., Zasadziński, J., Libura, W., Gronostajski, Z., Śliwa, R., Leszczyńska-Madej, B., Kaszuba, M., Woźnicki, A., Płonka, B., Widomski, P., & Madura, J. (2024). Latest advances in extrusion processes of light metals. *Archives of Civil and Mechanical Engineering 2024 24:3*, *24*(3), 1–53. https://doi.org/10.1007/S43452-024-00988-5

Li, X., Zhou, C., Overman, N., Ma, X., Canfield, N., Kappagantula, K., Schroth, J., & Grant, G. (2021). Copper carbon composite wire with a uniform carbon dispersion made by friction extrusion. *Journal of Manufacturing Processes*, *65*, 397–406. https://doi.org/10.1016/J.JMAPRO.2021.03.055

Liu, S., Sai, Q., Wang, S., & Williams, J. (2022). Effects of Laser Surface Texturing and Lubrication on the Vibrational and Tribological Performance of Sliding Contact. *Lubricants 2022, Vol. 10, Page 10*, *10*(1), 10. https://doi.org/10.3390/LUBRICANTS10010010

Liu, Y., Liu, W., & Xu, B. (2023). Fabrication of 3D Micro-electrode and Its Application in Micro-EDM. *Fabrication of Micro/Nano Structures via Precision Machining: Modelling, Processing and Evaluation*, 177–193. https://doi.org/10.1007/978-981-99-1338-1_8/TABLES/3

Ma, Y., Zhang, G., Cao, S., Huo, Z., Han, J., Ma, S., & Huang, Z. (2023). A Review of Advances in Fabrication Methods and Assistive Technologies of Micro-Structured Surfaces. *Processes 2023, Vol. 11, Page 1337*, *11*(5), 1337. https://doi.org/10.3390/pr11051337

MacGeough, J. A., Leu, M. C., Rajurkar, K. P., De Silva, A. K. M., & Liu, Q. (2001). Electroforming Process and Application to Micro/Macro Manufacturing. *CIRP Annals*, *50*(2), 499–514. https://doi.org/10.1016/S0007-8506(07)62990-4

Mahendran, S., Devarajan, R., Nagarajan, T., & Majdi, A. (2010). *A review of Micro-EDM*. https://www.scopus.com/inward/record.uri?eid=2-s2.0-79952434382&partnerID=40&md5=8e87851ed97a29666be317e0d3471b62

Malek, C. K., & Saile, V. (2004). Applications of LIGA technology to precision manufacturing of high-aspect-ratio micro-components and -systems: a review. *Microelectronics Journal*, *35*(2), 131–143. https://doi.org/10.1016/J.MEJO.2003.10.003

Manakari, V., Parande, G., & Gupta, M. (2016). Selective Laser Melting of Magnesium and Magnesium Alloy Powders: A Review. *Metals 2017, Vol. 7, Page 2*, *7*(1), 2. https://doi.org/10.3390/MET7010002

Max. (2025, February 18). *Pros and Cons of EDM: A Balanced Perspective*. https://proleantech.com/pros-and-cons-of-edm/

Ming, P. M., Zhu, D., Zhou, F., & Hu, Y. Y. (2010). Vacuum micro-electroforming technique for the production of void-free microcomponent. *Key Engineering Materials*, *426–427*, 142–146. https://doi.org/10.4028/WWW.SCIENTIFIC.NET/KEM.426-427.142

Moyer, J., Jackman, L. A., Adasczik, C., Davis, R., Forbes-Jones, R., Allvac, T., & P, O. (1998). *Advances in Triple Melting*. https://doi.org/10.7449/1994/SUPERALLOYS_1994_39_48.PDF

Newman, S. T., Nassehi, A., Xu, X. W., Rosso, R. S. U., Wang, L., Yusof, Y., Ali, L., Liu, R., Zheng, L. Y., Kumar, S., Vichare, P., & Dhokia, V. (2008). Strategic advantages of interoperability for global manufacturing using CNC technology. *Robotics and Computer-Integrated Manufacturing*, *24*(6), 699–708. https://doi.org/10.1016/J.RCIM.2008.03.002

Paul, S. (2022). *Binder Jetting of Aqueous Polyvinyl Alcohol for Additive Manufacturing of Inconel 718*. https://etheses.whiterose.ac.uk/id/eprint/31248/1/WhiteRoseSubmission_SP.pdf

Pimpin, A., & Srituravanich, W. (2011). Review on Micro- and Nanolithography Techniques and Their Applications. *Engineering Journal*, *16*(1), 37–56. https://doi.org/10.4186/ej.2012.16.1.37

Ramasawmy, H., & Blunt, L. (2004). Effect of EDM process parameters on 3D surface topography. *Journal of Materials Processing Technology*, *148*(2), 155–164. https://doi.org/10.1016/S0924-0136(03)00652-6

Schneider, R., Wiesinger, V., Gelder, S., & Reiter, G. (2023). Effect of the Slag Composition on the Process Behavior, Energy Consumption, and Nonmetallic Inclusions during Electroslag Remelting. *Steel Research International*, *94*(4), 2200483. https://doi.org/10.1002/SRIN.202200483;SUBPAGE:STRING:FULL

Shan, L., Kadhum, A. A. H., Al-Furjan, M. S. H., Weng, W., Gong, Y., Cheng, K., Zhou, M., Dong, L., Chen, G., Takriff, M. S., & Sulong, A. B. (2019). In Situ Controlled Surface Microstructure of 3D Printed Ti Alloy to Promote Its Osteointegration. *Materials 2019, Vol. 12, Page 815*, *12*(5), 815. https://doi.org/10.3390/MA12050815

Sharath, P. C. (2021). Multi directional forging: an advanced deforming technique for severe plastic deformation. *Advanced Welding and Deforming*, 529–556. https://doi.org/10.1016/B978-0-12-822049-8.00017-7

Sharma, S. K., Kumar, K. B., & Saxena, K. K. (2022). Micro Forming and its Applications: An Overview. *Key Engineering Materials*, *924*, 73–91. https://doi.org/10.4028/P-3U80QC

Shen, J., Imai, H., Chen, B., Ye, X., Umeda, J., & Kondoh, K. (2016). Deformation mechanisms of pure Mg materials fabricated by using pre-rolled powders. *Materials Science and Engineering: A*, *658*, 309–320. https://doi.org/10.1016/J.MSEA.2016.02.027

Sinanoğlu, C., Nair, F., & Karamiş, M. B. (2005). Effects of shaft surface texture on journal bearing pressure distribution. *Journal of Materials Processing Technology*, *168*(2), 344–353. https://doi.org/10.1016/J.JMATPROTEC.2005.02.252

Sole, M. J. (1994). Electroforming: Methods, materials, and merchandise. *JOM*, *46*(6), 29–35. https://doi.org/10.1007/BF03220715/METRICS

Song, J., Huang, H., Wang, X., & Shi, W. (2023). Status and prospects of surface texturing: design, manufacturing and applications. *Surface Science and Technology 2023 1:1*, *1*(1), 1–29. https://doi.org/10.1007/s44251-023-00022-5

Sugihara, T., & Enomoto, T. (2009). Development of a cutting tool with a nano/micro-textured surface—Improvement of anti-adhesive effect by considering the texture patterns. *Precision Engineering*, *33*(4), 425–429. https://doi.org/10.1016/J.PRECISIONENG.2008.11.004

Sulfur | S | CID 5362487 - PubChem. (n.d.). Retrieved 11 June 2025, from https://pubchem.ncbi.nlm.nih.gov/compound/Sulfur#section=Boiling-Point

Sung, S. Y., & Kim, Y. J. (2007). Melting and Casting of Titanium Alloys. *Materials Science Forum*, *539–543*, 3601–3606. https://doi.org/10.4028/WWW.SCIENTIFIC.NET/MSF.539-543.3601

Suris, J. A., Yurgel, C. C., & Alves de Sousa, R. (2023). Influence of the Grain-Flow Orientation after Hot Forging Process Evaluated through Rotational Flexing Fatigue

Test. *Metals 2023, Vol. 13, Page 187*, *13*(2), 187. https://doi.org/10.3390/MET13020187

Svetlizky, D., Das, M., Zheng, B., Vyatskikh, A. L., Bose, S., Bandyopadhyay, A., Schoenung, J. M., Lavernia, E. J., & Eliaz, N. (2021). Directed energy deposition (DED) additive manufacturing: Physical characteristics, defects, challenges and applications. *Materials Today*, *49*, 271–295. https://doi.org/10.1016/J.MATTOD.2021.03.020

Tala-Ighil, N., Maspeyrot, P., Fillon, M., & Bounif, A. (2007). Effects of surface texture on journal-bearing characteristics under steady-state operating conditions. *Proceedings of the Institution of Mechanical Engineers, Part J: Journal of Engineering Tribology*, *221*(6), 623–633. https://doi.org/10.1243/13506501JET287

Tam-Chang, S. W., & Iverson, I. (1999). Applications of Self-Assembled Monolayers (SAMs) of Alkanethiolates on Gold. *Studies in Surface Science and Catalysis*, *120*, 917–950. https://doi.org/10.1016/S0167-2991(99)80576-X

Taufiqurrakhman, M., Istiyanto, J., & Putra, N. (2021). Application of biomachining on copper for a minichannel heat exchanger. *Thermal Science and Engineering Progress*, *26*, 101128. https://doi.org/10.1016/J.TSEP.2021.101128

Uan, J. Y., & Cheng, H. F. (2007). Uniform Equiaxed Grain Structure throughout Thickness of a Hot-Rolled 5083 Al-Mg-Mn Alloy Thick Plate after a Tempering Treatment at 350°C. *MATERIALS TRANSACTIONS*, *48*(2), 178–183. https://doi.org/10.2320/MATERTRANS.48.178

Ullah, N., Rehan, M., Farooq, M. U., Li, H., Yip, W. S., & To, S. S. (2025). A comprehensive review of micro-milling: fundamental mechanics, challenges, and future prospective. *International Journal of Advanced Manufacturing Technology*. https://doi.org/10.1007/S00170-025-15388-Z

Vacuum Induction Melting Technology. (1987). *CMP Techcommentary*, *3*(3). https://p2infohouse.org/ref/09/08921.pdf#:~:text=Vacuum%20induction%20melting%20,result%20of%20VIM%2C%20the%20jet

Wei, Y., Resendiz, J., Tomkowski, R., & Liu, X. (2021). An Experimental Study of Micro-Dimpled Texture in Friction Control under Dry and Lubricated Conditions. *Micromachines 2022, Vol. 13, Page 70*, *13*(1), 70. https://doi.org/10.3390/MI13010070

Williamson, R. L., Schlienger, M. E., Hysinger, C. L., & Beaman, J. J. (1997). *Modern Control Strategies for Vacuum Arc Remelting of Segregation Sensitive Alloys*. 37–46. https://doi.org/10.7449/1997/SUPERALLOYS_1997_37_46

Wu, Z., Bao, H., Xing, Y., & Liu, L. (2021). Tribological characteristics and advanced processing methods of textured surfaces: a review. *The International Journal of Advanced Manufacturing Technology 2021 114:5*, *114*(5), 1241–1277. https://doi.org/10.1007/S00170-021-06954-2

Yadav, R., Dewang, Y., & Raghuvanshi, J. (2018). *A study on metal extrusion process*.

Yan, M. T., & Lin, S. S. (2011). Process planning and electrode wear compensation for 3D micro-EDM. *International Journal of Advanced Manufacturing Technology*, *53*(1–4), 209–219. https://doi.org/10.1007/S00170-010-2827-8/METRICS

Yin, B., Xu, B., Jia, H., Hua, X., & Fu, Y. (2022). Experimental research on the frictional performance of real laser-textured cylinder liner under different lubrication conditions. *International Journal of Engine Research*, *23*(4), 693–704. https://doi.org/10.1177/1468087421995293;JOURNAL:JOURNAL:JERA;REQUESTEDJOURNAL:JOURNAL:JERA;PAGE:STRING:ARTICLE/CHAPTER

Zanner, F. J. (2004). Vacuum Melting. *Encyclopedia of Materials: Science and Technology*, 1–6. https://doi.org/10.1016/B0-08-043152-6/01922-7

Zhang, H., Zhang, N., Gilchrist, M., & Fang, F. (2020). Advances in precision micro/nano-electroforming: a state-of-the-art review. *Journal of Micromechanics and Microengineering*, *30*(10), 103002. https://doi.org/10.1088/1361-6439/ABA017

Zhang, J., Chen, Y., Xu, B., Chao, Q., Zhu, Y., & Huang, X. (2018). Effect of surface texture on wear reduction of the tilting cylinder and the valve plate for a high-speed electro-hydrostatic actuator pump. *Wear*, *414–415*, 68–78. https://doi.org/10.1016/J.WEAR.2018.08.003

Zhang, J., Song, B., Wei, Q., Bourell, D., & Shi, Y. (2019). A review of selective laser melting of aluminum alloys: Processing, microstructure, property and developing trends. *Journal of Materials Science & Technology*, *35*(2), 270–284. https://doi.org/10.1016/J.JMST.2018.09.004

Zhou, S., Li, R., Jiang, S., & Huang, M. (2022). Hybrid periodic microstructures fabricated on chromium metal surface using ns-DLIP scanning combined with LIPSS. *Optics & Laser Technology*, *153*, 108261. https://doi.org/10.1016/J.OPTLASTEC.2022.108261

Zimniak, Z. (2020). A Constitutive Material Model Applied to Microforming Processes. *Materials 2020, Vol. 13, Page 5143*, *13*(22), 5143. https://doi.org/10.3390/MA13225143

APPENDICES

A. XRD Data

Pattern: PDF 33-0397 Radiation: 1.54060 Quality: Star (*)

Formula	FeCr0.29Ni0.16C0.06
Name	Chromium Iron Nickel Carbon
Name (mineral)	
Name (common)	304-stainless steel, austenite
Status	Primary
Ambient	Yes

d	2θ	I fix	h	k	l
2.07500	43.583	100	1	1	1
1.79610	50.792	45	2	0	0
1.26970	74.699	26	2	2	0
1.08280	90.697	30	3	1	1
1.03680	95.968	12	2	2	2
0.89790	118.161	3	4	0	0

Lattice:	Cubic	Mol. weight =	81.04
S.G.:	Fm-3m (225)	Volume [CD] =	46.31
		Dx =	
		Dm =	
		I/Icor =	-1.000

a =	3.59110		
a/b =	1.00000	Z =	4.00
c/b =	1.00000		

Color: Black
Analysis: Quantitative analysis by Atomic Absorption Spectroscopy: chromium 17.9%, nickel 11.4%, molybdenum <0.01%, silicon 0.88%, analysis incomplete
General Comments: Austenitic steel
General Comments: Synthetic taenite is Feich analog

Primary Reference
Publication: ICDD Grant-in-Aid
Authors: Pfoertsch, Ruud, Penn State University, University Park, Pennsylvania, USA.

Radiation:	CuKa	Filter:	M
Wavelength:	1.54060	d-spacing:	
SS/FOM:	F(6)= 56.1(0.0178, 6)		

Pattern: PDF 47-1405 Radiation: 1.54060 Quality: Indexed

Formula	Fe0.64Ni0.36
Name	Iron Nickel
Name (mineral)	
Name (common)	
Status	Primary
Ambient	Yes

Lattice:	Cubic	Mol. weight =	56.87
S.G.:	Fm-3m (225)	Volume [CD] =	46.35
		Dx =	
		Dm =	
		I/Icor =	-1.000

a =	3.59220		
a/b =	1.00000	Z =	4.00
c/b =	1.00000		

Sample Preparation: Formed by mechanical alloying of bimetallic layers

Primary Reference
Publication: Soviet Powder Metall. and Met. Ceramics
Detail: volume 30, page 606 (1991)
Authors: Samvelʹyan, R., Abovyan, E., Agbalyan, S., Manukyan, N., Sakanyan, M.

Radiation:	CoKa	Filter:	M
Wavelength:	1.54060	d-spacing:	
SS/FOM:	F(5)= 43.9(0.0230, 5)		

d	2θ	I fix	h	k	l
2.07400	43.605	100	1	1	1
1.79600	50.795	49	2	0	0
1.27000	74.679	25	2	2	0
1.08340	90.633	20	3	1	1
1.03730	95.907	7	2	2	2

Pattern: PDF 65-5131 Radiation: 1.54060 Quality: Calculated

Formula	Fe3Ni2
Name	Iron Nickel
Name (mineral)	
Name (common)	
Status	Primary
Ambient	Yes

Lattice:	Cubic
S.G.:	Fm-3m (225)

Mol. weight =	284.94
Volume [CD] =	46.58
Dx =	
Dm =	
I/Icor =	7.710

a =	3.59800		
a/b =	1.00000	Z =	0.80
c/b =	1.00000		

NIST M&A Collection Code: L 28729 14387 0
Temperature Factor: TF was not given, B set to 1.000 for calc
Sample Preparation: Ni(x)Fe(1-x) films with various compositions were vacuum deposited onto quartz-crystal substrates at room temperature by electron beam evaporating pellets of bulk Ni(y)Fe(1-y) alloys
Remark From ICSD/CSD: thin films; unit cell dimension taken from figure
Article Title: STRUCTURAL AND MAGNETIC PROPERTIES OF Ni(x)Fe(1-x) EVAPORATED THIN FILMS

Structure
Publication: J. Magn. Magn. Mater.
Detail: volume 67, page 55 (1987)
Authors: Dumpich, G., Wassermann, E. F., Manns, V., Keune, W., Murayama, S., Miyako, Y.

Primary Reference
Publication: Calculated from NIST using POWD-12++

Radiation:	CuKa1	Filter:	Not specified
Wavelength:	1.54060	d-spacing:	
SS/FOM:	F(8)= 999.9 (0.0004, 8)		

d	2θ	I fix	h	k	l
2.07731	43.532	999	1	1	1
1.79900	50.705	420	2	0	0
1.27209	74.535	170	2	2	0
1.08484	90.479	157	3	1	1
1.03865	95.742	43	2	2	2
0.89950	117.822	19	4	0	0
0.82544	137.879	60	3	3	1
0.80454	146.450	58	4	2	0

Pattern: PDF 44-1485 Radiation: 1.54060 Quality: Star (*)

Formula	NiFe2O4
Name	Nickel Iron Oxide
Name (mineral)	Trevorite, syn
Name (common)	
Status	Deleted
Ambient	Yes

Lattice:	Cubic	Mol. weight =	234.39
S.G.:	Fd-3m (227)	Volume [CD] =	579.95
		Dx =	
		Dm =	
		I/Icor =	3.500

a =	8.33930		
a/b =	1.00000	Z =	8.00
c/b =	1.00000		

Color: Black
Sample Preparation: Sample was prepared by firing NiO and 2 O3t 1200 C for 24 hours
General Comments: Average relative standard deviation in intensity of the ten strongest reflections for three specimen mounts = 12.5%.
Additional Pattern: Validated by calculated pattern
Optical Data: B=2.3
Deleted By or Rejected By: Deleted by 00-010-0325 which is satisfactory

Primary Reference
Publication: ICDD Grant-in-Aid
Authors: Sailer, R., McCarthy, G., North Dakota State University, Fargo, North Dakota, USA.

Radiation:	CuKa1	Filter:	M
Wavelength:	1.54060	d-spacing:	
SS/FOM:	F(22)= 105.2 (0.0084, 25)		

d	2θ	I fix	h	k	l
4.81300	18.419	12	1	1	1
2.94800	30.294	33	2	2	0
2.51400	35.685	100	3	1	1
2.40700	37.329	7	2	2	2
2.08500	43.363	23	4	0	0
1.91400	47.464	1	3	3	1
1.70200	53.819	9	4	2	2
1.60470	57.374	28	5	1	1
1.47420	63.003	34	4	4	0
1.40950	66.255	1	5	3	1
1.31860	71.490	2	6	2	0
1.27180	74.555	2	5	3	3
1.25700	75.586	1	6	2	2
1.20370	79.575	1	4	4	4
1.16780	82.541	1	7	1	1
1.11450	87.444	1	6	4	2
1.08560	90.398	3	7	3	1
1.04230	95.299	1	8	0	0
0.98280	103.216	1	6	6	0
0.96280	106.272	1	7	5	1
0.95640	107.301	1	6	6	2
0.93236	111.417	1	8	4	0

Pattern: PDF 84-0353 Radiation: 1.54060 Quality: Calculated

Formula	Ni2.44Ti.77O4
Name	Nickel Titanium Oxide
Name (mineral)	
Name (common)	
Status	Primary
Ambient	Yes

Lattice:	Cubic	Mol. weight =	244.11
S.G.:	Fd-3m (227)	Volume [CD] =	579.89
		Dx =	
		Dm =	
		I/Icor =	2.640

a =	8.33900	Z =	8.00
a/b =	1.00000		
c/b =	1.00000		

ICSD Collection Code: 201149
Temperature Factor: ITF
Article Title: Defect structure of the spinel Ni2.44 Ti.77 O4
Wyckoff Sequence: e d c a (FD3-MZ)
ANX: A3B10X16

Structure
Publication: J. Phys. Chem. Solids
Detail: volume 42, page 725 (1981)
Authors: Ambruster, T., Lager, G.A.

Primary Reference
Publication: Calculated from ICSD using POWD-12++

Radiation:	CuKa1	Filter:	Not specified
Wavelength:	1.54060	d-spacing:	
SS/FOM:	F(16)= 999.9 (0.0000, 17)		

d	2θ	I fix	h	k	l
4.81452	18.413	166	1	1	1
2.94828	30.291	233	2	2	0
2.51430	35.681	999	3	1	1
2.40726	37.325	315	2	2	2
2.08475	43.369	712	4	0	0
1.91310	47.487	21	3	3	1
1.70219	53.813	68	4	2	2
1.60484	57.369	260	5	1	1
1.47414	63.006	684	4	4	0
1.40955	66.253	15	5	3	1
1.31851	71.496	23	6	2	0
1.27169	74.563	66	5	3	3
1.25715	75.575	94	6	2	2
1.20363	79.581	76	4	4	4
1.16769	82.551	5	5	5	1
1.11435	87.459	23	6	4	2

Pattern: PDF 87-0262 Radiation: 1.54060 Quality: Calculated

Formula	Mn1.93Ni0.66Cu0.41O4
Name	Manganese Nickel Copper Oxide
Name (mineral)	
Name (common)	
Status	Primary
Ambient	Yes

Lattice:	Cubic	Mol. weight =	234.82
S.G.:	Fd-3m (227)	Volume [CD] =	583.96
		Dx =	
		Dm =	
		I/Icor =	4.740

a =	8.35850	Z =	8.00
a/b =	1.00000		
c/b =	1.00000		

ICSD Collection Code: 050289
Temperature Of Data Collection: REM TEM 27 C
Note: Rietveld profile refinement applied
Remark From ICSD/CSD: REM K slowly cooled sample
Temperature Factor: ITF
Article Title: Cation distribution and mechanism of electrical conduction in nickel-copper manganite spinels
Additional Pattern: See PDF 01-087-0264
Wyckoff Sequence: e d a (FD3-MS)
ANX: AB2X4

Structure
Publication: Solid State Ionics
Detail: volume 93, page 219 (1997)
Authors: Elbadraoui, E., Baudour, J.L., Bouree, F., Gillot, B., Fritsch, S., Rousset, A.

Primary Reference
Publication: Calculated from ICSD using POWD-12++

Radiation:	CuKa1	Filter:	Not specified
Wavelength:	1.54060	d-spacing:	
SS/FOM:	F(17)= 999.9 (0.0000, 17)		

d	2θ	I fix	h	k	l
4.82578	18.370	153	1	1	1
2.95518	30.219	347	2	2	0
2.52018	35.595	999	3	1	1
2.41289	37.234	79	2	2	2
2.08962	43.262	186	4	0	0
1.91757	47.370	1	3	3	1
1.70617	53.677	85	4	2	2
1.60859	57.223	303	5	1	1
1.47759	62.842	334	4	4	0
1.41284	66.079	10	5	3	1
1.39308	67.139	1	4	4	2
1.32159	71.304	24	6	2	0
1.27466	74.360	64	5	3	3
1.26009	75.368	30	6	2	2
1.20645	79.358	16	4	4	4
1.17042	82.316	6	5	5	1
1.11695	87.204	29	6	4	2

Pattern: PDF 84-0297 Radiation: 1.54060 Quality: Calculated

Formula	Ni2.62Ti0.69O4
Name	Nickel Titanium Oxide
Name (mineral)	
Name (common)	
Status	Primary
Ambient	Yes

Lattice:	Cubic	Mol. weight =	250.84
S.G.:	Fd-3m (227)	Volume [CD] =	580.43
		Dx =	
		Dm =	5.7
		I/Icor =	2.400

a =	8.34160		
a/b =	1.00000	Z =	8.00
c/b =	1.00000		

ICSD Collection Code: 201086
Test From ICSD: Calcul. formula slightly deviates from input
Test From ICSD: Charge sum slightly deviates from zero
Test From ICSD: At least one SOF implausible
Test From ICSD: At least one TF implausible
Temperature Factor: ITF
Article Title: Neutron poeder diffraction study of defect spinel structures: Tetrahedrally coordinated Ti4+ in Ni2.62 Ti0.69 O4 and Ni2.42 Ti0.74 Si0.05 O4
Wyckoff Sequence: e d c a (FD3-MZ)
ANX: A5B21X32

Structure
Publication: J. Appl. Crystallogr.
Detail: volume 14, page 261 (1981)
Authors: Lager, G.A., Armbruster, T., Ross, F.K., Rotella, F.J., Jorgensen, J.D.

Primary Reference
Publication: Calculated from ICSD using POWD-12++

Radiation:	CuKa1	Filter:	Not specified
Wavelength:	1.54060	d-spacing:	
SS/FOM:	F(16)= 999.9 (0.0000, 17)		

d	2θ	I fix	h	k	l
4.81603	18.407	236	1	1	1
2.94920	30.281	195	2	2	0
2.51509	35.669	979	3	1	1
2.40801	37.313	471	2	2	2
2.08540	43.354	999	4	0	0
1.91369	47.472	31	3	3	1
1.70272	53.795	57	4	2	2
1.60534	57.349	261	5	1	1
1.47460	62.984	866	4	4	0
1.40999	66.229	23	5	3	1
1.31892	71.470	19	6	2	0
1.27208	74.536	67	5	3	3
1.25754	75.548	142	6	2	2
1.20401	79.551	119	4	4	4
1.16806	82.519	9	5	5	1
1.11469	87.426	20	6	4	2

Pattern: PDF 89-7390 Radiation: 1.54060 Quality: Calculated

Formula	NiO
Name	Nickel Oxide
Name (mineral)	Bunsenite, syn
Name (common)	
Status	Primary
Ambient	Yes

Lattice:	Rhombo.H.axes	Mol. weight =	74.7
S.G.:	R-3m (166)	Volume [CD] =	54.65
		Dx =	
		Dm =	
		I/Icor =	4.740

a =	2.95492	Z =	3.00
c =	7.22658		
a/b =	1.00000		
c/b =	2.44561		

ICSD Collection Code: 076959
Temperature Of Data Collection: REM TEM 18 C
Remark From ICSD/CSD: REM M Cell at 90 K: 2.946, 60.2
Remark From ICSD/CSD: REM M Cubic NaCl-type above 523 K (=T(Neel)), cell at 548 K:
Remark From ICSD/CSD: REM (primitive rhombehedral cell: 2.9660, alpha=60.0
Remark From ICSD/CSD: REM M PDF 44-1159
Test From ICSD: No R value given
Test From ICSD: At least one TF missing
Article Title: Structure of nickel oxide
Wyckoff Sequence: b a (R3-MR)
ANX: AX

Structure
Publication: Nature (London)
Detail: volume 152, page 304 (1943)
Authors: Rooksby, H.B.

Primary Reference
Publication: Calculated from ICSD using POWD-12++

Radiation:	CuKa1	Filter:	Not specified
Wavelength:	1.54060	d-spacing:	
SS/FOM:	F(7)= 51.2(0.0137, 10)		

d	2θ	I fix	h	k	l
2.41226	37.244	570	1	0	1
2.41226	37.244	570	0	0	3
2.08834	43.290	999	0	1	2
1.47746	62.848	272	1	1	0
1.47590	62.922	279	1	0	4
1.25944	75.414	107	1	1	3
1.25944	75.414	107	0	1	5
1.20613	79.383	80	2	0	2
1.20443	79.517	37	0	0	6

Pattern: PDF 71-0855 Radiation: 1.54060 Quality: Calculated

Formula	NiMn.5Cr1.5O4
Name	Nickel Manganese Chromium Oxide
Name (mineral)	
Name (common)	nickel manganese
Status	Primary
Ambient	Yes

Lattice:	Cubic	Mol. weight =	228.16
S.G.:	Fd-3m (227)	Volume [CD] =	585.54
		Dx =	
		Dm =	
		I/Icor =	4.600

a =	8.36600		
a/b =	1.00000	Z =	8.00
c/b =	1.00000		

ICSD Collection Code: 009406
Test From ICSD: At least one TF missing
Article Title: Distribution Cationique et Distorsion Cristalline dans les Manganites Spinelles Ni Crx Mn2-x O4
Wyckoff Sequence: e d a (FD3-MZ)
ANX: AB2X4

Structure
Publication: J. Solid State Chem.
Detail: volume 5, page 250 (1972)
Authors: Renault, N., Baffier, N., Huber, M.

Primary Reference
Publication: Calculated from ICSD using POWD-12++

Radiation:	CuKa1	Filter:	Not specified
Wavelength:	1.54060	d-spacing:	
SS/FOM:	F(17)= 999.9 (0.0000, 17)		

d	2θ	I fix	h	k	l
4.83011	18.353	153	1	1	1
2.95783	30.191	331	2	2	0
2.52244	35.562	999	3	1	1
2.41506	37.200	73	2	2	2
2.09150	43.222	198	4	0	0
1.91929	47.325	1	3	3	1
1.70770	53.625	81	4	2	2
1.61004	57.167	287	5	1	1
1.47891	62.779	333	4	4	0
1.41411	66.012	10	5	3	1
1.39433	67.071	1	4	4	2
1.32278	71.230	23	6	2	0
1.27580	74.282	60	5	3	3
1.26122	75.289	26	6	2	2
1.20753	79.273	18	4	4	4
1.17147	82.227	6	5	5	1
1.11795	87.107	25	6	4	2

Pattern: PDF 89-5880 Radiation: 1.54060 Quality: Calculated

Formula	Ni7.6Mn0.2O8
Name	Nickel Manganese Oxide
Name (mineral)	
Name (common)	
Status	Primary
Ambient	Yes

Lattice:	Cubic	Mol. weight =	585.1
S.G.:	Fm-3m (225)	Volume [CD] =	582.08
		Dx =	
		Dm =	
		I/Icor =	4.990

a =	8.34950	Z =	4.00
a/b =	1.00000		
c/b =	1.00000		

ICSD Collection Code: 087107
Note: Rietveld profile refinement applied
Temperature Factor: ITF
Article Title: Relationship between crystal structure and electrical properties of murdochite-type Ni6+2x Mn1-x O8
Wyckoff Sequence: e d c b a (FM3-M)
ANX: A31X32

Structure
Publication: Solid State Commun.
Detail: volume 108, page 635 (1998)
Authors: Taguchi, H.

Primary Reference
Publication: Calculated from ICSD using POWD-12++

Radiation:	CuKa1	Filter:	Not specified
Wavelength:	1.54060	d-spacing:	
SS/FOM:	F(20)= 999.9 (0.0000, 20)		

d	2θ	I fix	h	k	l
4.82059	18.390	9	1	1	1
4.17475	21.266	4	2	0	0
2.95199	30.252	3	2	2	0
2.51747	35.634	3	3	1	1
2.41029	37.276	646	2	2	2
2.08737	43.311	999	4	0	0
1.91551	47.424	1	3	3	1
1.86700	48.735	1	4	2	0
1.70433	53.740	1	4	2	2
1.60686	57.290	1	5	1	1
1.47600	62.917	467	4	4	0
1.41132	66.159	1	5	3	1
1.39158	67.221	1	4	4	2
1.32017	71.392	1	6	2	0
1.27329	74.453	1	5	3	3
1.25873	75.464	158	6	2	2
1.20515	79.460	120	4	4	4
1.16916	82.424	1	5	5	1
1.15787	83.407	1	6	4	0
1.11575	87.322	1	6	4	2

Pattern: PDF 78-0644 Radiation: 1.54060 Quality: Calculated

Formula	Ni.95Cu.05O
Name	Nickel Copper Oxide
Name (mineral)	
Name (common)	
Status	Primary
Ambient	Yes

Lattice:	Cubic
S.G.:	Fm-3m (225)

Mol. weight =	74.94
Volume [CD] =	72.98
Dx =	
Dm =	
I/Icor =	4.780

a =	4.17890		
a/b =	1.00000	Z =	4.00
c/b =	1.00000		

ICSD Collection Code: 061545
Test From ICSD: No R value given
Test From ICSD: At least one TF missing
Article Title: Roentgenographische Untersuchungen an den Systemen MgO-CuO und NiO-CuO
Wyckoff Sequence: b a (FM3-M)
ANX: AX

Structure
Publication: Z. Anorg. Allg. Chem.
Detail: volume 332, page 230 (1964)
Authors: Schmahl, N.G., Barthel, J., Eikerling, G.F.

Primary Reference
Publication: Calculated from ICSD using POWD-12++

Radiation:	CuKa1	Filter:	Not specified
Wavelength:	1.54060	d-spacing:	
SS/FOM:	F(5)= 999.9 (0.0000, 5)		

d	2θ	I fix	h	k	l
2.41269	37.238	690	1	1	1
2.08945	43.266	999	2	0	0
1.47746	62.848	438	2	2	0
1.25999	75.375	144	3	1	1
1.20634	79.367	104	2	2	2

Pattern: PDF 43-0555 Radiation: 1.54060 Quality: Blank

Formula	Zn0.5Ni0.5FeCrO4
Name	Nickel Zinc Chromium Iron Oxide
Name (mineral)	
Name (common)	
Status	Primary
Ambient	Yes

Lattice:	Cubic
S.G.:	F (0)

Mol. weight =	233.88
Volume [CD] =	585.75
Dx =	
Dm =	
I/Icor =	-1.000

a =	8.36700		
a/b =	1.00000	Z =	8.00
c/b =	1.00000		

Sample Preparation: Prepared by heating a pelletized stoichiometric mixture of ZnO, NiO, 2 O3nd 2 O3or 20 hours at 500 C, then for 75 hours at 900 C

Primary Reference
Publication: Diffus. Defect Data
Detail: volume 53, page 409 (1987)
Authors: Khan, M., Al-Dallal, S., Ahmed, A.

Radiation:	CuKa	Filter:	F
Wavelength:	1.54060	d-spacing:	
SS/FOM:	F(7)= 5.1(0.1240, 11)		

d	2θ	I fix	h	k	l
2.94700	30.304	28	2	2	0
2.51700	35.641	100	3	1	1
2.40800	37.313	16	2	2	2
2.08800	43.298	38	4	0	0
1.70200	53.819	15	4	2	2
1.60600	57.324	48	5	1	1
1.47700	62.870	82	4	4	0

Pattern: PDF 30-0865 Radiation: 1.54060 Quality: Star (*)

Formula	Ni3TiO5/3NiO·TiO2
Name	Nickel Titanium Oxide
Name (mineral)	
Name (common)	
Status	Primary
Ambient	Yes

Lattice:	Tetragonal	Mol. weight =	304
S.G.:	I41/amd (141)	Volume [CD] =	289.59
		Dx =	
		Dm =	
		I/Icor =	-1.000

a =	5.89400
c =	8.33600
a/b =	1.00000
c/b =	1.41432

Sample Preparation: Prepared at 1400 C by heating rutile Ti O2)nd NiO, and quenched
General Comments: Stable only above 1390 C
General Comments: Single crystal data taken

Primary Reference
Publication: Neues Jahrb. Mineral., Monatsh.
Authors: Werner, H., Gebert.

Radiation:	MoKa1	Filter:	Not specified
Wavelength:	1.54060	d-spacing:	
SS/FOM:	F(13)= 37.8 (0.0115, 30)		

d	2θ	I fix	h	k	l
4.81000	18.431	12	1	0	1
2.94600	30.315	25	2	0	0
2.51400	35.685	100	1	0	3
2.40700	37.329	31	2	0	2
2.08500	43.363	45	0	0	4
1.91300	47.490	2	2	1	3
1.70200	53.819	6	2	0	4
1.60500	57.363	20	1	0	5
1.47400	63.013	50	2	2	4
1.31900	71.465	4	1	1	6
1.27200	74.541	9	3	0	5
1.25600	75.656	10	4	2	2
1.20400	79.551	8	4	0	4